Journal Pre-proof

Testbed results for scalar and vector radiative transfer computations of light in atmosphere-ocean systems

Jacek Chowdhary , Peng-Wang Zhai , Feng Xu , Robert Frouin , Didier Ramon

PII: S0022-4073(19)30370-X
DOI: https://doi.org/10.1016/j.jqsrt.2019.106717
Reference: JQSRT 106717

To appear in: *Journal of Quantitative Spectroscopy & Radiative Transfer*

Received date: 28 May 2019
Revised date: 16 October 2019
Accepted date: 22 October 2019

Please cite this article as: Jacek Chowdhary , Peng-Wang Zhai , Feng Xu , Robert Frouin , Didier Ramon , Testbed results for scalar and vector radiative transfer computations of light in atmosphere-ocean systems, *Journal of Quantitative Spectroscopy & Radiative Transfer* (2019), doi: https://doi.org/10.1016/j.jqsrt.2019.106717

This is a PDF file of an article that has undergone enhancements after acceptance, such as the addition of a cover page and metadata, and formatting for readability, but it is not yet the definitive version of record. This version will undergo additional copyediting, typesetting and review before it is published in its final form, but we are providing this version to give early visibility of the article. Please note that, during the production process, errors may be discovered which could affect the content, and all legal disclaimers that apply to the journal pertain.

© 2019 Published by Elsevier Ltd.

Highlights:

- Vector radiative transfer computations were performed for atmosphere-ocean models
- Four models, four wavelengths, two altitudes, and 100 geometries were considered
- Three radiative transfer codes were used to validate the accuracy of computations
- Tabulated testbed values are presented for Stokes parameters *I*, *Q*, and *U*
- The accuracy of the testbed tables is at least 10^{-5} and mostly better than 10^{-6}

Journal Pre-proof

Title Page

Manuscript Title:

Testbed results for scalar and vector radiative transfer computations of light in atmosphere-ocean systems

Type

Full-length article

Authors:

Jacek Chowdhary [a, 1] , Peng-Wang Zhai [b] , Feng Xu [c, 2] , Robert Frouin [d] , Didier Ramon [e]

[a] Department of Applied Physics and Applied Mathematics, Columbia University, 2880 Broadway, New York, NY 10025, USA, jacek.chowdhary@nasa,gov

[b] Joint Center for Earth Systems Technology/Department of Physics, University of Maryland, Baltimore County, 1000 Hilltop Circle Baltimore, MD 21250, USA

[c] Jet Propulsion Laboratory, California Institute of Technology, Mail Stop 233-200, 4800 Oak Grove Drive, Pasadena, California, CA 91109, USA

[d] Scripps Institution of Oceanography, University of California San Diego, 9500 Gilman Drive #0224, La Jolla, California, CA 92093-0224, USA

[e] HYGEOS, Euratechnologies, 165 avenue de Bretagne, 59000 Lille, France

[1] **Corresponding author**

[2] **Present address**: School of Meteorology, The University of Oklahoma, National Weather Center, Suite 5900, 120 David L. Boren Blvd., Norman, Oklahoma, OK 73072, USA

Keywords:

radiative transfer, atmosphere-ocean system, Stokes parameters, testbed, polarimeters, PACE

Declaration of interest:

None

Supplementary material

- Tables of scattering matrix elements and of testbed reflectance values
- Figures of numerical spread in testbed reflectance values

Journal Pre-proof

Journal Pre-proof

Testbed results for scalar and vector radiative transfer computations of light in atmosphere-ocean systems

Jacek Chowdhary, Peng-Wang Zhai, Feng Xu, Robert Frouin, Didier Ramon

Abstract

We generate and tabulate reflectance values of the Stokes parameters *I*, *Q*, and *U* of upwelling radiance above a rough ocean surface and at the top of the atmosphere (TOA) for 100 scattering geometries, four atmosphere-ocean systems, and four wavelengths. The atmosphere-ocean systems increase in complexity from *(a)* a molecular atmosphere above a rough ocean surface (*AOS-I* model); to *(b)* a pure water body below a rough ocean surface (*AOS-II* model); to *(c)* a fully-coupled simple atmosphere-ocean system (*AOS-III* model) containing a molecular atmosphere, rough ocean surface, and pure water; to *(d)* a fully-coupled complex atmosphere-ocean system (*AOS-IV* model) that includes scattering by molecules, rough ocean surface, pure water, and hydrosols. Our wavelengths (350, 450, 550, and 650 nm) capture the ultraviolet-visible. Our tables provide radiative transfer (RT) testbed results for atmosphere-ocean systems with an accuracy that surpasses the measurement accuracy of state-of-the-art polarimeters. To validate the accuracy of these tables we performed computations using three independent RT codes that provide deterministic numerical solutions for the RT equation. The agreement is 10^{-5} for *AOS-IV* model, and 10^{-6} for the other models. The degree of linear polarization computed by these RT codes differs by ≤0.2% for 15 isolated cases of tabulated reflectance values, and by ≤0.1% for all remaining cases. We also provide comparisons with results obtained by a stochastic RT code for *AOS-I* model. The agreement between the deterministic and stochastic results for this model is 10^{-5} at TOA, and 10^{-6} above the ocean surface.

Keywords:
radiative transfer, atmosphere-ocean system, Stokes parameters, testbed, polarimeters, PACE

1. Introduction

Unpolarized incident light that is scattered by particles suspended in a medium becomes partially polarized. Most of this polarization is linearly orientated (i.e., oriented along a constant direction that is perpendicular to the propagation of light). The degree and direction of this polarization changes with the viewing angle and wavelength of observation for a given sample of suspended particles. Such angular and spectral polarization signatures are also highly sensitive to the physical and chemical properties of the suspended particles [1]. This sensitivity has successfully been exploited during the last 40+ years to obtain unique

Journal Pre-proof

information about aerosols and clouds in planetary atmospheres from moderately accurate polarimetric remote sensing observations of extraterrestrial planets such as Venus [2,3,4,5,6,7,8,9], Jupiter [10,11,12], Titan [13,14] and of the Earth [15,16,17,18]. In addition, promising results have been obtained in analyzing the sensitivity of polarimetric remote sensing observations over oceans to properties of hydrosols [19,20,21]. Currently available airborne polarimeters are able to measure linear polarization signatures with up to an order of magnitude better accuracy [22,23,24,25], which allows for better characterization of aerosol properties [26,27]. Such measurement improvements are necessary for future space-borne polarimeters to reduce the estimate uncertainty of – and therefore to increase our understanding of – climate change caused by anthropogenic aerosols [28,29]. The measurement improvements can also lead to new data products, such as the composition of ocean microlayer surfaces [30]. Another ocean application of such improvements, recognized by the Pre-Aerosol Cloud ocean Ecosystem (PACE) science teams (ST), is to better distinguish and invert atmospheric scattering from ocean color contributions in space-borne observations of complex atmosphere-ocean environments [31,32,33]. However, the improvements in polarimetric remote sensing capabilities require also matching improvements in the validation of simulation accuracy for upwelling polarized light above the ocean surface in realistic atmosphere-ocean systems.

The current literature contains a multitude of testbed results to validate radiative transfer (RT) computations for the polarization of light in isolated slabs of atmosphere. Tabulated results can be found for homogeneous atmospheres containing molecules only [12,34,35,36,37], for (in-) homogeneous atmospheres containing (molecules and) aerosols [38,39,40], and for homogeneous atmospheres consisting of cloud droplets [40]. However, while *Escribano et al.* [41] do consider an ocean surface below an atmosphere for testbed results, there exist no such tables for the polarization of light computed for atmosphere-ocean system (AOS) models that include water-leaving radiance. Comparisons for polarized light computations using different RT codes have been reported for such models [42,43,44,45,46], but the results are *drawn* as a function of viewing angle which limits the accuracy that can be extracted to validate other RT codes. Current and future remote sensing polarimeters can measure the degree of linear polarization (*DLP*) to an accuracy of 0.2%–0.5%, which requires that the RT codes used to analyze these measurements must be validated to at least the same accuracy. Even quantitative RT results for just the intensity of light computed for AOS models are rare to find [47,48].

The main objective of this study is to provide accurate (down to at least 10^{-5}) tabulated results and comparisons for the reflectance of total and linearly polarized upwelling radiance just above the ocean surface (SRF) and at the top of the atmosphere (TOA) computed for different viewing geometries, wavelengths, and AOS models. Such accuracies are necessary to obtain numerical threshold accuracies for *DLP* of better than 0.2%. Our target will be to obtain numerical accuracies for *DLP* of better than 0.1%. A secondary objective is to provide corresponding results for radiance-only computations, which also do not yet exist at the time of this study. We employ one thoroughly-vetted RT code (i.e., *eGAP*) to compute all tabulated values, and two additional thoroughly-vetted RT codes (i.e., *MarCh-AD* and *SOS-CAOS*) to assess their associated uncertainties. The RT computations are performed by members of the current term (2014-2017) PACE Science Team who are tasked to investigate the improvement that can be achieved in atmospheric correction for space-borne ocean color photometry when adding multi-angle, multi-spectral polarimetric remote sensing data [49,50,51]. The viewing geometries for the tabulated results include the backscattering and sunglint observations in the solar principal plane, and off-principal plane observations that

Journal Pre-proof

graze neutral polarization points seen in actual airborne observations [52] and in simulations [53,54]. The wavelength for the tabulated results ranges from 350 to 650 nm to include the UV-VIS hyperspectral observations considered for the PACE mission [31]. Four AOS models are considered for our computations (**Table 1**). They increase gradually in complexity from *(a)* a purely molecular atmosphere above a wind-ruffled ocean surface without (i.e., totally transparent) ocean body (*AOS-I* model); to *(b)* a pure ocean water body below a wind-ruffled ocean surface with no (i.e., totally transparent) atmosphere (*AOS-II* model); onward to *(c)* a fully-coupled simple atmosphere-ocean system body (*AOS-III* model) containing a molecular atmosphere, wind-ruffled ocean surface and pure ocean water; and finally to *(d)* a fully-coupled complex atmosphere-ocean system (*AOS-IV* model) that includes scattering by molecules, wind-ruffled ocean surface, pure ocean water, and sharply forward-peaked scattering by hydrosols. Some results presented for the *AOS-I* model can be compared with those reported for an isolated molecular atmosphere by *Natraj et al.* [36] if the optical thickness is set to 0.5 (this model is denoted by *AOS-I**), whereas the purpose of the advanced *AOS-IV* model is to produce realistic water-leaving radiance contributions to SRF and TOA observations. Note however that none of our AOS models reproduce the complexity encountered in the real world, i.e. their microscopic and macroscopic properties are chosen to facilitate comparisons of RT computations rather than for use in actual ocean color inversions. When possible though, we provide references for the interested reader to find more realistic values for the ocean parameters used in our AOS models.

The organization of this manuscript is as follows. In Sec. 2, we review basic definitions that are specific for the results reported in this work. The following Sec. 3 provides the details of the AOS models and their properties used as input for our RT computations. The RT codes used to perform our computations are described in Sec. 4. In Sec. 5 we discuss our RT results, and compare the spread in numerical results between our RT codes. The corresponding tables and figures are provided separately as supplementary material at doi:10.1019/j.jqsrt.2019.XX.XXX; see Appendix A for details. In what follows, we will reference them with a '**S**' preceding the table or figure number. Finally, we summarize our work in Sec. 6.

2. Definitions for scattering geometries and polarization quantities

Consider the atmosphere-ocean system in **Fig. 1** (also provided as **Fig. S1** in supplementary material). that is illuminated by the Sun in the direction of $\boldsymbol{k}_0$, and that is scattering light towards a viewer in the direction of $\boldsymbol{k}$. In what follows, we will use subscript '0' to denote direct sunlight quantities. To quantify directions $\boldsymbol{k}_0$ and $\boldsymbol{k}$, we use a right-handed Carthesian coordinate system whose positive z-axis points towards the upward direction in the atmosphere and whose positive x-axis aligns along the shadow of the z-axis. The direction $\boldsymbol{k}_0$ can then be quantified by the pair of angles (ϑ_0,φ_0), where ϑ_0 is the polar zenith angle (i.e. angle between $\boldsymbol{k}_0$ and the positive z-axis) and φ_0 is the polar azimuth angle (i.e. angle between the positive x-axis and the projection of $\boldsymbol{k}_0$ upon the xy plane, measured clockwise when looking upwards). Similarly, $\boldsymbol{k}$ can be quantified by the pair of polar angles (ϑ,φ) defined in the same manner as (ϑ_0,φ_0) except for considering the direction and projection of $\boldsymbol{k}$. Note that $\varphi_0 = 0^\circ$ because of the convention chosen in this study for the x-axis. Furthermore, to simplify future notation we define $\theta_0 \equiv \pi - \vartheta_0$.

The intensity and state of polarization of a beam of light traveling in the direction of $\boldsymbol{k}$. can be described by the (4×1) Stokes vector $\boldsymbol{I}$ given by

$$\boldsymbol{I} = \begin{pmatrix} I \\ Q \\ U \\ V \end{pmatrix} \tag{1}$$

which has as its components Stokes parameters *I*, *Q*, *U*, and *V*. Stokes parameter *I* describes the intensity of a quasi-monochromatic beam of light travelling in one direction. Part of this beam of light can be linearly polarized, the properties of which are described by Stokes parameters *Q* and *U*. The fraction of light that is linearly polarized (referred to in this work as the degree of linear polarization, or *DLP*) is given by

$$DLP = 100 \times \frac{\sqrt{Q^2+U^2}}{I}\ \%. \tag{2}$$

Modern polarimetric remote sensing instruments can measure *DLP* with accuracies between 0.2 and 0.5% [22,23,24,25]; hence, one of the (threshold) objectives of this work is to at least match the 0.2% measurement accuracy with numerical computations for light that is multiply scattered in atmosphere-ocean systems. Our target for these computations is to obtain numerical accuracies for *DLP* that are better than 0.1%. We will report numerical results for Stokes parameters *I*, *Q*, *U*, as a function of θ_0, ϑ, and φ for various atmosphere-ocean systems. Another part of light can be circularly polarized which is described by Stokes parameter *V*. The corresponding fraction of light that is circularly polarized is given by $|V|/I$. While we include *V* in our computations, we do not report results for this Stokes parameter because it very small and routinely ignored in airborne and spaceborne polarization measurements.

We refer to *Hovenier and van der Mee* [55] for a more detailed discussion on the definition and properties of Stokes parameters *I*, *Q*, *U* and *V*. Here, we remark on a few specific choices made in the present work. The value and sign of Stokes parameter *Q* (and *U*) depends on *(i)* the reference plane *M* chosen to define parallel and perpendicular directions, and *(ii)* the convention chosen to denote parallel or perpendicular. For example, the *value* of *Q* describes the part of light that is linearly polarized either along or perpendicular to plane *M*, whereas the *sign* of *Q* is used to indicate parallel or perpendicular. In this work, we use the meridian plane (i.e. the vertical plane containing the beam of light – see **Fig. 1**) for the reference plane *M*, and use the positive sign of *Q* to define parallel to plane *M*. Note that our sign convention is the same as used by *van de Hulst* [56], but that it differs from the one chosen by *Coulson et al.* [34] and *Natraj et al.* [36]. However, the degree of linear polarization *DLP* in Eq. (2) does not depend on the choices made for plane *M* and for the sign conventions [1].

3. Atmosphere-ocean system properties

Our RT simulation studies are performed for four AOS models that are numbered in increasing order to denote increasing complexity in their components and/or RT computations (**Table 1**). The setup is designed to start with two simple models that allow for consideration

Journal Pre-proof

of radiation that has been scattered between the ocean surface and a molecular atmosphere (*AOS-I* model), and between the ocean surface and a molecular ocean body (*AOS-II* model). Note that results presented for *AOS-I* model can be compared with the tabulated results provided by *Natraj et al.* [36] for isolated molecular atmospheres if the molecular optical thickness τ_{mol} is set to 0.5. We will refer to *AOS-I** model for these particular results. The results for *AOS-III* model allow for consideration of radiation that has interacted with all three model components. This is followed by *AOS-IV* model where hydrosols have been added to the ocean of *AOS-III* model.

The constituents of the ocean component (if present) and of the atmosphere component (if present) are vertically homogeneous. The specification for *AOS-IV* model resembles cases of real atmosphere-ocean systems, but even this model oversimplifies oceanic (e.g., no vertical distribution and no bottom) and atmospheric scattering properties (e.g., no vertical distribution and no aerosols). We will alert the reader whenever we adopt such simplifications.

Four wavelengths λ are considered for the RT simulation studies of each AOS model: λ = 350 nm, 450 nm, 550 nm, and 650 nm. The open ocean is brightest for the former two wavelengths when containing least amount of plankton particles (which absorb strongly at 443 nm), and brightest for the latter two wavelengths when containing a lot of plankton particles. Mineral particles can brighten the ocean even more for the latter two wavelengths, but such particles are not included in our AOS models. In addition to these 4 wavelengths, we consider the case of τ_{mol} = 0.5 for *AOS-I** model (see discussion above) which corresponds to $\lambda \approx 370$ nm. The following subsections specify the spectral radiative properties for the components of our AOS models.

3.1. Ocean body properties

To perform RT computations for the underwater light in AOS models *AOS-II* to *AOS-IV*, one has to specify three quantities for their homogeneous ocean body components:

(i) the scattering matrix $\boldsymbol{F}_{blk}$ for the bulk ocean body volume element (Sec. 3.1.1);
(ii) the single scattering albedo ω_{blk} for the bulk ocean body volume element (Sec. 3.1.2);
(iii) the ocean extinction optical thickness τ_{blk} for the ocean body layer (Sec. 3.1.3).

3.1.1 Scattering matrix $\boldsymbol{F}_{blk}$

The bulk ocean body scattering matrix $\boldsymbol{F}_{blk}$ can be written as

$$\boldsymbol{F}_{\mathrm{blk}} \equiv \boldsymbol{F}_{\mathrm{blk}}(\lambda, \Theta) = \frac{b_{\mathrm{w}}(\lambda)\boldsymbol{F}_{\mathrm{w}}(\Theta) + b_{\mathrm{p}}(\lambda)\boldsymbol{F}_{\mathrm{p}}(\Theta)}{b_{\mathrm{w}}(\lambda) + b_{\mathrm{p}}(\lambda)} \tag{3}$$

where Θ is the scattering angle, $b_w(\lambda)$ and $\boldsymbol{F}_w(\Theta)$ are the scattering coefficient and scattering matrix for pure seawater, and $b_p(\lambda)$ and $\boldsymbol{F}_p(\Theta)$ are the scattering coefficient and scattering matrix for marine particles, respectively. The spectral values for $b_w(\lambda)$ vary also with the

Journal Pre-proof

temperature and salinity of seawater (see e.g. [57,58] and references therein), but for simplicity we choose for our simple RT case computations the tabulated variation with λ given in *Smith and Baker* [59] (see **Table 2**). Scattering matrix $\boldsymbol{F}_w(\Theta)$ can be modeled using Rayleigh scattering with a depolarization factor δ_w for pure water. The value commonly used for δ_w ranges from 0.039 [60,61,62], to 0.051 [57,63], to 0.09 [64,65]. For the sake of simplicity, we choose $\delta_w = 0$ for our simple RT case computations. The values for $b_p(\lambda)$ and $\boldsymbol{F}_p(\Theta)$ depend on the composition of hydrosols particles. The International Ocean Colour Coordinating Group (IOCCG) report #5 (http://www.ioccg.org/reports/report5.pdf, hereafter referred to as *IOCCG5*) identifies two types of hydrosol particles, phytoplankton and non-algae (detritus and minerals) denoted by subscripts 'ph' and 'dm' , whose contributions to $b_p(\lambda)$ and $\boldsymbol{F}_p(\Theta)$ can be written as

$$b_{\mathrm{p}}(\lambda) = b_{\mathrm{ph}}(\lambda) + b_{\mathrm{dm}}(\lambda) \tag{4}$$

and

$$\boldsymbol{F}_{\mathrm{p}}(\Theta) = \frac{b_{\mathrm{ph}}(\lambda)\boldsymbol{F}_{\mathrm{ph}}(\Theta) + b_{\mathrm{dm}}(\lambda)\boldsymbol{F}_{\mathrm{dm}}(\Theta)}{b_{\mathrm{dm}}(\lambda) + b_{\mathrm{dm}}(\lambda)}. \tag{5}$$

In *IOCCG5* the *average* spectra of $b_{ph}(\lambda)$ and $b_{dm}(\lambda)$ change with the Chlorophyll *a* concentration [Chl]. However, these spectra are allowed to fluctuate for any given [Chl] by up to an order of magnitude. Furthermore, *IOCCG5* prescribes only the *(1,1)* elements of matrices $\boldsymbol{F}_{ph}(\Theta)$ and $\boldsymbol{F}_{dm}(\Theta)$.

As an alternative, we choose for our RT test case computations the scattering coefficients and matrices for detritus-plankton (D-P) mixtures given by *Chowdhary et al.* [54,66]. Their approach uses the bio-optical model developed by *Morel and Maritorena* [67] for open ocean waters to constrain the particulate coefficients and scattering function, i.e.

$$b_{\mathrm{p}}(\lambda) = 0.347\,[\mathrm{Chl}]^{0.766}\left(\frac{660}{\lambda}\right)^{k} \tag{6}$$

where *k* is made to vary with [Chl], and

$$\tilde{b}_{\mathrm{b,p}} \equiv 2\pi \int_{0.5\pi}^{\pi} \frac{F_{\mathrm{p}}(\Theta)}{4\pi} \sin\Theta \, d\Theta = 0.002 + 0.01(0.50 - 0.25\log_{10}[\mathrm{Chl}]) \tag{7}$$

where $\tilde{b}_{b,p}$ is the particulate backscattering ratio. Note that Eq. (5) assumes scattering matrix $\boldsymbol{F}_p(\Theta)$ to be spectrally invariant which is consistent with data analysis findings reported by *Whitmire et al.* [68] and *Huot et al.* [69], although exceptions have been observed [70,71]. The factor of $(4\pi)^{-1}$ appears here because we follow *Hansen and Travis* [1] when normalizing $F_p(\Theta)$, i.e.

$$\int_{4\pi} \frac{F_{\mathrm{p}}(\Theta)}{4\pi} \, d\Omega = 1 \tag{8}$$

Journal Pre-proof

where $d\Omega$ is an infinitesimal element of a sold angle. To obtain $\boldsymbol{F}_{\mathrm{p}}(\Theta)$, *Chowdhary et al.* [66] first write

$$\boldsymbol{F}_{\mathrm{p}}(\Theta) = \frac{\{1-f_{\mathrm{dm}}\}\sigma_{\mathrm{ph}}F_{\mathrm{ph}}(\Theta)+f_{\mathrm{dm}}\sigma_{\mathrm{dm}}F_{\mathrm{dm}}(\Theta)}{\{1-f_{\mathrm{dm}}\}\sigma_{\mathrm{ph}}+f_{\mathrm{dm}}\sigma_{\mathrm{dm}}} \tag{9}$$

where σ_{ph} and σ_{dm} are the scattering cross sections of phytoplankton and detritus (non-algae) particles, $\boldsymbol{F}_{\mathrm{ph}}(\Theta)$ and $\boldsymbol{F}_{\mathrm{dm}}(\Theta)$ are the corresponding scattering matrices, and f_{dm} is the fraction of total number of particles that is detritus. Phytoplankton and detritus class values for $\{\sigma_{\mathrm{ph}},\boldsymbol{F}_{\mathrm{ph}}(\Theta)\}$ and $\{\sigma_{\mathrm{dm}},\boldsymbol{F}_{\mathrm{dm}}(\Theta)\}$ are then obtained from Mie computations that *(i)* use realistic hydrosol refractive indices and size distributions for each class, and *(ii)* are constrained by the linear polarization for pure seawater. This leads to many viable solutions (denoted as "members") for each class. Note that variations of $\boldsymbol{F}_{\mathrm{p}}(\Theta)$ with particle inhomogeneity [72,73,74] and with particle morphology [75,76,77] are ignored in these computations. Finally, a member of the phytoplankton class is mixed with a member of the detritus class (creating a so-called D-P mixture) such that Eq. (7) is satisfied. Note that the particle mixing fraction f_{dm} in Eq. (9) varies with [Chl], and is also unique for each D-P mixture. **Table 2** provides the scattering coefficients from Eq. (6). **Table 3** provides the particle properties of the phytoplankton and detritus members chosen for our simple RT case computations, and the corresponding cross sections (assuming λ = 550 nm for all cases) and mixture values that are used to mix their matrices in Eq. (9). A small [Chl] value is chosen for the two shortest wavelengths, and a large [Chl] value for the two longest wavelengths, to maximize the water-leaving radiance at all wavelengths. We reiterate that the class members in **Table 3** represent simplified, extreme models of phytoplankton and detritus particles chosen so that their mixtures can reproduce a very broad range of bulk ocean particulate backscattering ratios from 0.0027 to 0.044 [66] while preserving realistic polarized water-leaving radiances [54]. The corresponding *non-zero* scattering matrix elements for $\boldsymbol{F}_{\mathrm{p}}(\Theta)$ (divided by 4π as in Eq. (8)) are provided in **Table S1a** and **Table S1b** (see supplementary material) for small and large [Chl] values, respectively. The asymmetry parameter (as defined for Table 2 in *Chowdhary et al.* [54]) for the phase functions of these matrices is 0.95 and 0.97, respectively

3.1.2 Single scattering albedo $\boldsymbol{\omega}_{\mathrm{blk}}$

The bulk ocean body scattering albedo ω_{blk} can be written as

$$\omega_{\mathrm{blk}} \equiv \omega_{\mathrm{blk}}(\lambda) = \frac{b_{\mathrm{w}}(\lambda)+b_{\mathrm{p}}(\lambda)}{b_{\mathrm{w}}(\lambda)+b_{\mathrm{p}}(\lambda)+a_{\mathrm{blk}}(\lambda)} \tag{10}$$

where $a_{\mathrm{blk}}(\lambda)$ is the bulk ocean absorption coefficient. The ocean body for AOS models *AOS-II* and *AOS-III* consists of pure seawater; hence for these models $b_{\mathrm{p}}(\lambda) = 0$, and $a_{\mathrm{blk}}(\lambda)$ becomes the absorption coefficient $a_{\mathrm{w}}(\lambda)$ for pure seawater:

$$a_{\mathrm{blk}}(\lambda) = a_{\mathrm{w}}(\lambda)\ . \tag{11a}$$

Journal Pre-proof

Values for $a_w(\lambda)$ can be found in the literature [78,79] (reproduced in **Table 2**). Note that these values ignore variations with salinity and with temperature [80,81,82]. The ocean body for AOS model *AOS-IV* includes particulate and dissolved matter; hence for these studies we use Eq. (6) for $b_p(\lambda)$ and

$$a_{\mathrm{blk}}(\lambda) = a_{\mathrm{p}}(\lambda) + a_{\mathrm{y}}(\lambda) + a_{\mathrm{w}}(\lambda)\ . \tag{11b}$$

In Eq. (11b), $a_p(\lambda)$ and $a_y(\lambda)$ are the absorption coefficients for marine particles and colored dissolved organic matter ("yellow substance"), respectively. The *IOCCG5* decomposes $a_p(\lambda)$ into $a_{ph}(\lambda)$ and $a_{dm}(\lambda)$ for phytoplankton and non-algal particles, respectively, and provides average spectra for $a_{ph}(\lambda)$, $a_{dm}(\lambda)$, and $a_y(\lambda)$ as a function of [Chl]. However, these spectra are allowed to fluctuate for any given [Chl] by up to several factors. Furthermore, they only provide $a_{ph}(\lambda)$ values for wavelengths larger than 400 nm, although these values are currently extended to include UV wavelengths [49]. As a simple alternative, we use the bulk ocean absorption coefficients $a_{blk}(\lambda)$ for the D-P mixtures given by *Chowdhary* [54] (reproduced in **Table 2**). Their $a_{blk}(\lambda)$ spectra are computed from the bulk ocean downward irradiance attenuation coefficient K_{blk} that are provided by *Morel and Maritorena* [67] as a function of [Chl] and for wavelengths between 350-700 nm. *Morel et al.* [83] used a larger set of measurements to update their K_{blk} values; however, these updated values are not publically available and are therefore not shown in **Table 2**. We use the same small [Chl] value for the two shortest wavelengths, and the same large [Chl] value for the two longest wavelengths, as for the $\boldsymbol{F}_p(\Theta)$ discussed in Sec. 3.1.1.

3.1.3 Extinction optical thickness τ_{blk}

If the bulk ocean body is homogeneous, then its extinction optical thickness τ_{blk} can be written as

$$\tau_{\mathrm{blk}} \equiv \tau_{\mathrm{blk}}(\lambda) = \{a_{\mathrm{blk}}(\lambda) + b_{\mathrm{p}}(\lambda) + b_{\mathrm{w}}(\lambda)\} \times \Delta z \tag{12}$$

where Δz is the physical thickness of the ocean body. For simplicity, we choose Δz = 100 m for all our RT study cases. The corresponding values for τ_{blk} are given in **Table 2**. The bottom below this ocean body is assumed black.

3.2. Ocean surface properties

We use the wind-ruffled, surface slope probability distribution $p(\mu_n,\varphi_n)$ given by *Cox and Munk* [84]. Here $\mu_n \equiv \cos(\theta_n)$, and (θ_n,φ_n) denotes the pair of polar zenith and azimuth angle (see Sec. 2 for polar angle definitions) of the surface slope normal. For simplicity, we choose for our RT simulation studies the isotropic (wind-direction independent) version of $p(\mu_n,\varphi_n)$, i.e.

$$p(\mu_{\mathrm{n}}, \varphi_{\mathrm{n}}) = \frac{1}{\pi\chi^2\mu_{\mathrm{n}}^3}\exp\left(-\frac{1-\mu_{\mathrm{n}}^2}{\chi^2\mu_{\mathrm{n}}^2}\right) \tag{13}$$

Journal Pre-proof

where

$$\chi^2 = 0.003 + 0.00512 \times W \tag{14}$$

relates the surface slope variance χ^2 to the windspeed W (m/s) at 12.5 meters above the ocean surface. We choose $\chi^2 = 0.03884$ (see **Table 4**) which corresponds to $W \approx 7$ m/s. This ocean surface model ignores the impact on skylight reflection of wind-*directional* surface roughnesses [85]. We further ignore shadowing and multiple surface facet scattering effects [86,87,88], do not include surface foam [89,90,91,92,93], and do not modify the surface reflection and transmission to force conservation of energy [94]. The corresponding reflection and transmission matrices for the ocean surface are computed using the geometrical optics approach. The ocean surface refractive index m_w for these computations is 1.34 for all wavelengths, i.e. we also ignore the variation of m_w with wavelength, salinity, and temperature ([61] and references therein).

3.3. Atmosphere properties

To perform RT computations for the skylight light in AOS models *AOS-I*, *AOS-I** and *AOS-III* to *AOS-IV*, one has to specify three quantities for their homogeneous atmospheres:

(i) the scattering matrix $\boldsymbol{F}_{atm}$ for the atmosphere volume element (Sec. 3.3.1);
(ii) the single scattering albedo ω_{atm} for the atmosphere volume element (Sec. 3.3.2);
(iii) the extinction optical thickness τ_{atm} for atmosphere layer (Sec. 3.3.3);

3.3.1 Scattering matrix $\boldsymbol{F}_{atm}$

The atmosphere in AOS models *AOS-I*, *AOS-I**, *AOS-III* and *AOS-IV* contains only molecules, which means that

$$F_{atm} \equiv F_{atm}(\Theta) = F_{mol}(\Theta) \tag{15}$$

where $\boldsymbol{F}_{mol}$ is the scattering matrix for molecules. Scattering matrix $\boldsymbol{F}_{mol}$ can be modeled using Rayleigh scattering with a depolarization factor δ_m for atmospheric gases [1]. Note that δ_m varies with the composition of gases and with wavelength [95], but we will assume δ_m=0 for all our RT case computations.

3.3.2 Single scattering albedo ω_{atm}

The spectrum of $\omega_{atm}(\lambda)$ will depend on the presence and amount of absorbing matter in the atmosphere. For the molecular atmospheres of AOS models *AOS-I*, *AOS-I**, *AOS-III* and *AOS-IV*, $\omega_{atm}(\lambda)$ will therefore vary with gases in the atmosphere that absorb between 350 and 650 nm such as water vapor H_2O, nitrogen dioxide NO_2 and ozone O_3 [96,97]. For our

Journal Pre-proof

RT test case computations we ignore the presence of such gases, i.e. the molecular single scattering albedo $\omega_{mol}(\lambda)$ for these computations is set to 1. That implies that there are no absorbing constituents in the atmosphere component of our AOS models; hence,

$$\omega_{atm} \equiv \omega_{atm}(\lambda) = \omega_{mol}(\lambda) = 1 \tag{16}$$

for all our AOS models (see **Table 5a**,**b**).

3.3.3 Extinction optical thickness τ_{atm}

The extinction optical thickness τ_{atm} for the molecular atmospheres of AOS models *AOS-I*, *AOS-I**, *AOS-III* and *AOS-IV* is identical to the molecular extinction optical thickness $\tau_{mol}(\lambda)$ for these atmospheres:

$$\tau_{atm} \equiv \tau_{atm}(\lambda) = \tau_{mol}(\lambda)\,. \tag{17}$$

For $\tau_{mol}(\lambda)$, we follow *Bodhaine et al.* [95] who provide tabulated values of $\tau_{mol}(\lambda)$ between 250 and 1000 nm. An exception is made for *AOS-I**, where we set τ_{mol} = 0.5. The results for $\tau_{mol}(\lambda)$ are shown in **Table 5a** for *AOS-I* to *AOS-IV*, and in **Table 5b** for *AOS-I**.

4. Radiative transfer codes

The following sections provide summaries for the RT codes used in this study. The first three RT codes (*eGAP*, *MarCH-AD*, and *SOS-CAOS*) provide deterministic numerical solutions for the vector radiative transfer equation, and are used to compute (*eGAP*) and validate (*MarCH-AD* and *SOS-CAOS*) our tabulated reflectance values. The fourth RT code (*SMART-G*) is used to illustrate comparisons with probabilistic solutions for the vector radiative transfer equation. References are provided for detailed information on the RT methods, and brief descriptions are given for AOS configurations, unique RT features, and validation efforts. **Table 6** summarizes current RT simulation options and computations for each RT code.

4.1 NASA/GISS RT code: *eGAP*

The extended General Adding Program (*eGAP*) RT code used at NASA/GISS for atmosphere-ocean systems is based on the doubling/adding method that is described by *de Haan et al.* [38] for polarized light scattered by isolated atmospheres, and that was extended by *Chowdhary* [94] to include polarized light scattering in ocean systems (see also [66]). It provides parameters *I*, *Q*, *U* and *V* of Stokes vector ***I*** for the up- and down-welling light at any level in an atmosphere that is illuminated from above by the Sun and bounded from below by an ocean system. The user-provided accuracy ε for solving the adding equations [38] is set to 10^{-7} for the present study. The code-embedded accuracy for numerically expanding the ocean surface matrices in Fourier series is better than 10^{-6} (this estimation is based on increasing the number of Gaussian quadrature points for the azimuthal integration).

Journal Pre-proof

The AOS is assumed plane-parallel and horizontally homogenous. Inelastic (e.g. Raman) scattering processes are ignored in *eGAP* computations. The atmosphere is divided into layers of aerosol/cloud particles and/or molecules. The scattering properties of particles, which may be nonsperical [98,99], are provided by the user for each separate layer. The ocean component consists of a wind-ruffled ocean surface [84], an ocean body (optional), and an ocean bottom (optional). The ocean body is divided into separate layers as well and contains water, marine particle matter, and marine dissolved matter. The scattering and absorption properties of marine matter for each layer, which may come from measurements (e.g., [100,101,102]), are provided by the user. The ocean bottom is assumed Lambertian with a user-specified albedo.

Special RT features include the possibility to decompose computations for Stokes vector $\boldsymbol{I}$ into scattering contributions of light that has interacted with

(1a) only the atmosphere component;
(1b) both the atmosphere and ocean surface components;
(1c) only the ocean surface component (i.e. the sunglint);
(1d) both the ocean surface and ocean body components;
(1e) all three AOS components (atmosphere, ocean surface and ocean body).

Other user-provided options for RT computations include

(2) perform scalar RT (i.e. ignore Q, U, and V) or 3×3 RT (i.e. ignore V) computations;
(3) include wave shadowing, foam, and/or wind-directionality for rough ocean surface;
(4) account for energy impacted by wave shadowing and/or multiple wave scattering;
(5) specify number of quadrature points separately for aerosol and hydrosol scattering;
(6) specify the desired accuracy ε of RT computations.

Finally, *eGAP* provides exact (i.e. *not* interpolated or average) RT results for any pre-specified viewing geometry using the supermatrix formalism described in *de Haan et al.* [38].

The computations performed by *eGAP* for AOS models were validated internally by *(i)* verifying (within 1×10^{-6}) conservation of energy for a conservatively scattering system; *(ii)* verifying (for 12 digits) matrix symmetry relationships for reflection by vertically inhomogeneous systems [103]; and *(iii)* verifying (for 12 digits) the computation of ocean surface reflection and transmission properties using 2 different methods (the geometric optics approach [104] and the Kirchhoff approximation [26]. External validations consisted of verifying (for ≥4 digits) our RT results with those computed by other RT codes for *(iv)* isolated atmospheres [38,105]; *(v)* an atmosphere above a rough ocean surface [43]; *(vi)* a rough ocean surface above a molecular ocean [42]; and (*v*) a molecular atmosphere above a rough ocean surface with a molecular ocean body [45].

4.2 NASA/JPL RT codes*: MarCh-AD*

The hybrid Markov-Chain-Adding-Doubling (*MarCh-AD*) code was developed by *Xu et al.* [106] to compute polarized RT in a coupled atmosphere-ocean system. Two different RT

Journal Pre-proof

methods are integrated in one computational scheme to enhance the computational efficiency: the Markov chain (*MarCh*) method for optically inhomogeneous atmosphere system and the doubling method for homogeneous ocean system. The *MarCh* method can apply to the ocean system as well when its vertical profile need to be accounted. The RT fields from the atmosphere and ocean systems as well as the reflected/transmitted light fields across the rough ocean/atmosphere interface are coupled by use of a revised "adding" strategy [106]. As one of the major algorithm components, the *MarCh* method was first developed by *Esposito and House* [107] to compute scalar (intensity only) radiative transfer in a plane-parallel atmosphere and then vectorized to calculate the full Stokes vector components (including *I*, *Q*, *U*, and *V*] for an atmosphere overlying a depolarizing or a partially polarizing surface [108,109]. It is featured by matrix algebra, which helps gain efficiency in computing RT in a vertically inhomogeneous medium [110] and lends the code readily to implementation on a graphics processing unit (GPU) for future high-speed computations. As a recent development, the *MarCh-AD* code was coupled into an optimization scheme for a simultaneous retrieval of aerosol and water properties [106].

To use the *MarCh-AD* code in a coupled atmosphere-ocean system (CAOS), the optical depth and scattering/absorption properties of atmospheric and oceanic constituents including aerosols, air molecules, absorbing gas, hydrosol particles, CDOM, and pure seawater need to be input (cf. Secs. 3.1 and 3.3 for details). In addition, the wind speed is input to calculate the reflection and transmission of light across an ocean surface based on Cox-Munk model [42,84]. Depending on the desired accuracy, several options are provided and need to be specified in the configuration file. They include *a)* RT run in scalar or vector modes; *b)* use of full or 3 by 3 approximate scattering matrix for polarized single scattering by atmospheric and oceanic constituents; *c)* number of streams and Fourier terms; and *d)* inclusion or exclusion of shadowing effect [86,111] and wind direction.

Numerical validation of *MarCh-AD* code for a CAOS system includes *(i)* energy conservation test for a conservatively scattering system; *(ii)* verification of matrix symmetry relationships for the polarized reflected light from a plane-parallel medium [103]; and (*iii*) comparison with the *SOS-CAOS* solutions for several cases of a Rayleigh atmosphere covering an ocean with a Chlorophyll *a* concentration of 0.3 mg/m^3 and a set of sea-surface wind speeds [42]. The relative difference in reflectance computed by the two codes is less than ~0.2% for most scattering geometries, and the absolute difference in degree of linear polarization is less than ~0.002.

4.3 UMBC RT code: *SOS-CAOS*

The Successive Order of Scattering method for Coupled Atmosphere-Ocean System (*SOS-CAOS*) was developed by *Zhai et al.* [42,112]. In this method, the total radiance field is decomposed into contributions from different order of scattering. The single scattering contribution is obtained analytically and the radiance field of each higher order of scattering can be evaluated from the radiance field of one less order of scattering. This process is repeated iteratively until the higher order of scattering contribution is negligible. Sensitivity study shows that a total number of scattering order 40 provides sufficient accuracy for most practical applications [42]. The scattering medium in the atmosphere and ocean are assumed to be plane-parallel and macroscopically mirror-symmetric, i.e., the scattering matrices are block-diagonal. For phase functions with elongated forward scattering peak, the Delta-*m*

Journal Pre-proof

[113] or Delta-fit [114] methods are used to truncate the phase function while keeping the reduced scattering matrix unchanged [112]. To reduce the error introduced in the truncation schemes, the single scattering solution for the AOS uses the un-truncated original phase function [115].

The ocean surface can be either flat or rough, in the latter case the isotropic Cox-Munk wave slope distribution is used to calculate the reflection and transmission matrices of the air-sea interface [42,84]. Surface shadowing effect can be taken into account with the shadowing function [86,111]. All four Stokes parameters *I*, *Q*, *U*, *V* are computed at arbitrary vertical levels, in either the atmosphere or ocean. The parameters *I*, *Q*, *U*, *V* at arbitrary viewing angles are obtained from the iteration of source matrix methods [116,117]. In addition to using an AOS model, the *SOS-CAOS* RT code can be easily configured to numerically solve the vector radiative transfer equation for atmosphere – surface system with the surface reflection specified by the surface reflection models [118,119]. In addition to the elastic scattering, the *SOS-CAOS* code also solves the polarized radiation field due to the inelastic Raman scattering [120,121] and fluorescence [122] for ocean waters.

The validation of the *SOS-CAOS* RT code has been performed against available benchmark data for atmosphere-surface system [34,40]. For the AOS with a flat ocean, the code is compared with the Monte Carlo solution [123]. For the AOS with rough ocean surface, the Stokes parameters are compared with the *eGAP* solution [66]. All the comparisons have achieved relative differences around the order of 0.1% for radiance. The differences for the polarized ratio *Q/I*, *U/I*, and *V/I* are smaller than 10^{-4} for all the cases considered. Moreover, the code has gone through various self-consistence tests including energy conservation, single scattering limit solution, and asymptotic behavior.

4.4 HYGEOS RT code: *SMART-G*

SMART-G (Speed-up Monte-Carlo Advanced Radiative Transfer code with GPU) is a radiative transfer solver for the coupled ocean-atmosphere system with a wavy interface (*Ramon et al.*, [124]). It is based on the Monte-Carlo technique, works in either plane-parallel or spherical-shell geometry, and accounts for polarization. The vector code is written in CUDA (Compute Unified Device Architecture) and runs on GPUs (Graphic Processing Units). Physical processes included in the current version of the code are the elastic scattering, absorption, reflection, and refraction. The atmosphere and ocean are considered as 1-dimensional stratified media with layers characterized by gaseous optical depth and single scattering albedo (case of atmosphere), Rayleigh phase matrix, and particle (aerosol, hydrosol, and/or cloud droplet/crystal) optical depth, single scattering albedo, and phase matrix. The ocean can be infinitely deep or bounded by a Lambertian reflective bottom at finite depth.

The wavy interface can be modelled in two ways: *(i)* as a purely reflecting interface whose BRDF is obtained by the combination of the isotropic wave slope distribution [84] and the Fresnel reflection matrix. In that case the direction of the reflected photons is sampled according to a Lambertian law and the photon statistical weight is multiplied by the BRDF [125], and *(ii)* by sampling the wave slope and azimuth according to a distribution law based on Cox & Munk isotropic wave slope distribution but now depending on the photon incident zenith angle [126]. This procedure results in some slopes hiding [127]. Then Fresnel

Journal Pre-proof

reflection (resp. transmission) is applied to the reflected (resp. transmitted) photon Stokes vector. In both cases the light intensity is eventually modulated by a wave shadowing function [128]. The wave direction sampling method *(ii)* allows for multiple reflection at the air sea interface. In the AOS comparison exercise, the BRDF method *(i)* has been used for consistency with other codes.

The radiances at any level of the domain can be estimated using the local estimate variance reduction method [129]. Benchmark values are accurately reproduced for clear [37] and cloudy [40] atmospheres over a wavy reflecting surface and a black ocean [46]. For pure Rayleigh atmospheres as in AOS comparisons, the agreement is better than 10^{-5} in intensity and 0.1% in degree of polarization [124]. In the pure cloud case the convergence of the code is slowed down with the local estimate method. This is due to the presence of highly peaked phase functions, as described in *Buras and Mayer* [130]. These authors proposed variance reduction techniques to mitigate the problem. Such techniques are not yet implemented in the code.

The main advantage of the *SMART-G* code is the possibility to introduce easily increasing complexity in the system, like for example wave heights, horizontal inohomogeneities of the albedo like adjacency effects, or 3-dimensional variations of the oceanic/atmospheric optical properties. Its traditional drawbacks, the speed and Monte Carlo noise is counterbalanced by the use of massive parrallelization on GPU, which for a given machine typically speeds up by two orders of magnitude the computation time compared with a sequential algorithm running on CPUs.

5. Radiative transfer computations and discussion

5.1 Viewing geometries and altitudes

To include and exclude sunglint contaminations in our RT computations for *AOS-I* to *AOS-IV* models, we consider 2 Sun angles θ_0 (i.e., θ_0 = 30°, 60°), 13 equidistant viewing zenith angles ϑ covering the range between 0°–60° (i.e., ϑ = 0°, 5°, …, 55°, 60°), and 2 full azimuth planes at 0° and 60° from the principal plane (i.e., φ = 0° & 180°, and 60° & 240°). Note that φ = 0° and 180° correspond to viewing the sunglint and backscattering direction, respectively (see **Fig. 1**). These azimuth angles provide good test cases for validating *AOS-II* model computations of the polarization maximum and minima, respectively, seen in previous computations for water-leaving radiance [66]. Computations for viewing azimuth angles φ = 60° and 240° provide additional good test cases for validating *AOS-I*, *AOS-III* and *AOS-IV* model computations of large and small polarization values, respectively, seen in previous results for airborne upwelling radiance outside the sunglint [52,53,54]. In total, 100 different scattering geometries are considered for each of these AOS models at a given wavelength and altitude. From Sec. 3, we recall that four wavelengths are considered for each AOS model. In addition, we consider two altitudes for each AOS model: just above the surface (SRF) to simulate ship-based measurements, and at the top of the atmosphere (TOA) to simulate space-borne measurements. Note *AOS-I* model has no atmosphere; hence, the SRF and TOA results are the same for this model. In summary, we use 800 different view/altitude/wavelength

combinations in our computations for each Stokes parameter and for each *AOS-I*, *AOS-II* *AOS-II* and *AOS-IV* model.

For *AOS-I** model we perform another set of computations, i.e. for *(i)* a different set of Sun angles ($\mu_0 \equiv |\cos\theta_0| = 0.6$) and viewing angles ($\mu \equiv |\cos\vartheta| = 0.02, 0.10, 0.16, 0.20, 0.28, 0.32, 0.40, 0.52, 0.64, 0.72, 0.84, 0.92, 1.00$); and *(ii)* only TOA observations. These conditions are identical those used by *Natraj et al.* [36] for benchmark computations of Stokes parameters *I*, *Q*, and *U* for the radiance reflected by an isolated molecular atmosphere. Hence, the radiative impact of adding an ocean surface to a molecular atmosphere can be studied by comparing our results for *AOS-I** model with those provided by *Natraj et al.* [36]. The latter results are recomputed and provided as well in this work for the reader's convenience.

5.2 Accuracy considerations

5.2.1 Deterministic RT results

The number N_{atm} of Gaussian quadrature points used for the numerical computations of skylight (i.e., for radiative transfer of upward or downward light in the atmosphere, if present) is set to 30. This number is more than sufficient to account for molecular scattering in the atmosphere (i.e., increasing N_{atm} does not affect the results for *AOS-I*). The number N_{sea} of Gaussian quadrature points used for numerical computations of underwater light (i.e., for radiative transfer of upward or downward light within the ocean, if present) is decoupled from N_{atm} in the *eGAP* RT model (Sec. 4.1). That is, the light propagation directions represented by the N_{sea} Gaussian points do not coincide with the N_{atm} directions of skylight refracted by the ocean surface. Hence the number N_{sea} of Gaussian quadrature points required to obtain convergence for the computation of water-leaving radiance will now depend on *(i)* the bulk ocean body scattering matrix $\boldsymbol{F}_{blk}$ in Eq. (3), and *(ii)* the ocean surface slope probability distribution $p(\mu_n,\varphi_n)$ in Eq. (13). For AOS models *AOS-II* and *AOS-III* where $\boldsymbol{F}_{blk}$ is equal to scattering matrix $\boldsymbol{F}_w(\Theta)$ for pure seawater, convergence in numerical results is driven by $p(\mu_n, \varphi_n)$. Here, N_{sea} is set to 80 to obtain convergence for the water-leaving radiance within 1×10^{-6}. For AOS model *AOS-IV*, $\boldsymbol{F}_{blk}$ contains the sharp diffraction peak of particulate scattering matrix $\boldsymbol{F}_p(\Theta)$ (see **Tables S1a,b** in supplementary material) which leads to an asymmetry parameter of 0.95 for [Chl] = 0.03 mg/m^3 and 0.97 for [Chl] = 3.00 mg/m^3 for the corresponding phase function [54].This in turn requires higher values of N_{sea} to obtain numerical convergence. Brute force *scalar* radiative transfer computations with the *eGAP* RT model (Sec. 4.1) show that the water-leaving radiance converges within 1×10^{-6} if N_{sea} approaches 900. Such computations require excessive computer memory allocation and become prohibitively time consuming when including polarization. These computational burdens can be alleviated by reducing N_{sea} and carefully renormalizing $\boldsymbol{F}_p(\Theta)$ to properly constrain the resulting energy loss while keeping the decrease in accuracy at a minimum. The *eGAP* RT code (Sec. 4.1) normalizes Fourier expansion components of $\boldsymbol{F}_p(\Theta)$ for the forward and backward scattering zenith directions [94], whereas the *MarCh-AD* RT code (Sec. 4.2) and *SOS-CAOS* RT code (Sec. 4.3) use the Delta truncation methods [113,131] to modify the diffraction peak of $\boldsymbol{F}_p(\Theta)$. Scalar RT computations show that these approaches allow the corresponding water-leaving radiance to be computed within an accuracy of 1×10^{-5} if N_{sea} is

Journal Pre-proof

set to 300. In what follows, we adopt this value of N_{sea} and renormalize $\boldsymbol{F}_p(\Theta)$ in all our RT computations for AOS model *AOS-IV*.

5.2.2 Probabilistic RT results

The general form of the estimator for the Stokes vector $\boldsymbol{I}$ at level z in the local estimate direction is given by the sum of the different contributions $\vec{s}_n^l$ of each photon n, after each interaction $l < l^{max}$ (that can be scattering, transmission, and reflection at the surface or at the sea floor) :

$$I = \frac{1}{N_p} \sum_{n=1}^{N_p} \sum_{l=1}^{l^{max}(n)} w_n^l \, \vec{s}_n^l \tag{18}$$

where N_p is the total number of photons launched in the simulation, l^{max} is the total number of interaction of each photon, and w_n^l is the statistical weight of each photon just before interaction l. Those weights are computed for correcting the biases introduced in the various random samplings. They are close to 1 in case of optimal sampling, like the wave slope sampling, but could depart significantly from unity in the case of the BRDF method described in Sec. 4.4. $\vec{s}_n^l$ estimates depend on the probabilities of a particular interaction *at* a given place *in* a given direction. Apart from N_p, for which we have a total control, the relative variance of the Stokes vector is thus mainly dependent on the variance of the weights and the relative variance of the $\vec{s}_n^l$ contributions, which themselves depend on the viewing geometry and level z. For example the contribution from photons reflected at the surface has an increasing relative variance with increasing viewing angles as the range of BRDF values experienced by all incident photons is getting larger. In a pure Rayleigh atmosphere, the scattering contributions exhibit a low relative variance because of the smoothness of the Rayleigh phase function. Thus the ratio of atmospheric to surface contribution influences the relative variance of the estimates, and we expect lower relative standard deviations for estimates at the TOA than for estimates at SRF. Error bars given hereafter for *SMART-G* correspond to the estimation of the absolute standard deviations of the Stokes parameters computed from Eq. (18), with N_p=3.10^{11}.

5.3 Testbed results

Table S2 in the supplementary material shows for the observations specified in Sec 5.1 the normalized upwelling intensity quantities $R_{I,comp}$, $R_{Q,Vector}$, $R_{U,Vector}$ computed by *eGAP* for AOS model *AOS-I*. In what follows, subscript 'comp' stands for 'Scalar' or 'Vector' to denote results obtained from scalar (i.e., excluding all polarization) or full vector (i.e., including linear *and* circular polarization) computation, respectively. The normalization used for these radiance quantities leads to reflectance quantities, i.e.

$$R_{I,comp} \equiv \frac{\pi I_{comp}}{S_0 \mu_0}, \tag{19a}$$

Journal Pre-proof

$$R_{\mathrm{Q,Vector}} \equiv \frac{\pi Q_{\mathrm{Vector}}}{S_0 \mu_0}, \tag{19b}$$

$$R_{\mathrm{U,Vector}} \equiv \frac{\pi U_{\mathrm{Vector}}}{S_0 \mu_0} \tag{19c}$$

where S_0 is the TOA extraterrestrial solar flux and $\mu_0 = |\cos\theta_0|$. For simplicity, we set $S_0 = \pi$. **Tables S3**, **S4**, and **S5** show the same reflectance quantities for AOS models *AOS-II*, *AOS-III*, and *AOS-IV*, respectively. Following the discussion on numerical accuracy in Sec. 5.2, the expected accuracy for the results reported in **Tables S2** to **S4** is 10^{-6} while for **Table S5** it is 10^{-5}.

The top row of **Table S6** provides the same TOA reflectance quantities as in **Table S2** except for *(i)* multiplying these quantities by μ_0 (i.e. showing Stokes parameters for an extraterrestrial solar flux of π), and *(ii)* using AOS model *AOS-I** (i.e. using the same viewing geometries and molecular optical as in [36]. Furthermore, like *Natraj et al.* [36] we do not perform scalar computations for *AOS-I** model. The corresponding expected accuracy for all results in this table is 10^{-6}. The bottom row of **Table S6** show the same Stokes parameters as the top row except for ignoring the ocean surface in the RT computations for *AOS-I**. The latter row shows therefore the same quantities as *Natraj et al.* [36] except that our difference in sign convention for Stokes parameter Q causes our Q values to have the opposite sign (see discussion in Sec. 2). We remark further that, apart from this difference in sign, all our results in the bottom row agree within $\leq 10^{-6}$ of those reported by *Natraj et al.* [36] which is consistent with our value for the adding/doubling accuracy ε (Sec. 4.1) and for N_{atm}.

5.4 Spread in results obtained from different RT codes

5.4.1 AOS-I model

The diagrams in **Figs. S2a–S2l** (first and third row) that are provided in the supplementary material show for AOS model *AOS-I* the absolute differences $d_{\mathrm{abs}}(R_{\mathrm{I,Vector}})$, $d_{\mathrm{abs}}(R_{\mathrm{Q,Vector}})$, and $d_{\mathrm{abs}}(R_{\mathrm{U,Vector}})$ for the computation of reflectance $R_{\mathrm{I,Vector}}$, $R_{\mathrm{Q,Vector}}$, and $R_{\mathrm{U,Vector}}$, respectively, when using the *MarCh-AD*, *SOS-CAOS* and *SMART-G* RT codes described in Secs. 4.2 to 4.4. These differences are obtained as follows:

$$d_{\mathrm{abs}}(R_{\mathrm{I,Vector}}) \equiv R_{\mathrm{I,Vector}}^{\mathrm{Model}} - R_{\mathrm{I,Vector}}^{\mathrm{Table}}, \tag{20a}$$

$$d_{\mathrm{abs}}(R_{\mathrm{Q,Vector}}) \equiv R_{\mathrm{Q,Vector}}^{\mathrm{Model}} - R_{\mathrm{Q,Vector}}^{\mathrm{Table}}, \tag{20b}$$

$$d_{\mathrm{abs}}(R_{\mathrm{U,Vector}}) \equiv R_{\mathrm{U,Vector}}^{\mathrm{Model}} - R_{\mathrm{U,Vector}}^{\mathrm{Table}} \tag{20c}$$

where on the right-hand side the first term (i.e., R^{Model}) are the reflectance values computed from one of the RT codes described in Secs. 4.2–4.4 and the second term (i.e., R^{Table}) are the reflectance values reported in **Table S2**. Note that the left-hand ordinate (vertical) axes in

Journal Pre-proof

Figs. S2a–S2l (first and third row) denote the differences for the *MarCh-AD* and *SOS-CAOS* results, whereas the right-hand ordinate axes (which are an order of magnitude larger) denote the differences for the *SMART-G* results. We further remark that the reflectance results from *MarCh-AD* and *SOS-CAOS* RT computations are obtained down to 10^{-7} (as opposed to 10^{-6} for the reflectance results from *eGAP* computations; see Sec. 4.1). Therefore the $d_{\text{abs}}(R)$ differences for *MarCh-AD* and *SOS-CAOS* depict the sum of *(i)* numerical reflectance differences with *eGAP* computations; and *(ii)* round-off residuals for the reflectance values in **Table S2**. Hence when the numerical results for the *MarCh-AD* and *SOS-CAOS* computations approach each other down to 10^{-7}, then their $d_{\text{abs}}(R)$ differences shown in **Fig. S2** become equal to one another and likely *depict only round-off residuals* for the reflectance values in **Table S2**. This can be clearly seen, e.g., for $d_{\text{abs}}(R_{\text{Q,Vector}})$ in **Fig. S2d**.

The yellow bars in the diagrams in **Figs. S2a– S2l** (first and third row) depict an absolute uncertainty of $\pm 10^{-6}$ using the left ordinate axis, and of $\pm 10^{-5}$ using the right ordinate axis, for the $R_{\text{I,Vector}}$, $R_{\text{Q,Vector}}$, and $R_{\text{U,Vector}}$ reflectance values in **Table S2**. Note that, except for 18 isolated cases, the absolute RT code reflectance differences $d_{\text{abs}}(R_{\text{I,Vector}})$, $d_{\text{abs}}(R_{\text{Q,Vector}})$ and $d_{\text{abs}}(R_{\text{Q,Vector}})$ plotted in these figures for *MarCh-AD* and *SOS-CAOS* remain less than $\pm 1.5\times 10^{-6}$ (see left ordinate axis) for all 2,400 comparison cases, i.e., for all 800 viewing/altitude/wavelength combinations multiplied by three Stokes parameters. The 18 exceptions occur for *SOS-COAS* results, but the corresponding absolute reflectance differences still remain within $\pm 2\times 10^{-6}$. In what follows, we will use bold-faced fonts in our testbed tables to mark such exceptions. However note that, after performing extensive tests for these few exceptions, we stand by the stated uncertainty of $\pm 10^{-6}$ for all values given in our testbed tables (including those for scalar computations) unless noted otherwise.

The absolute reflectance differences $d_{\text{abs}}(R_{\text{I,Vector}})$, $d_{\text{abs}}(R_{\text{Q,Vector}})$ and $d_{\text{abs}}(R_{\text{U,Vector}})$ plotted in the same diagrams for *SMART-G* (see right ordinate axes in first and third row in **Figs. S2a–S2l**) remain for all 1,200 SRF comparison cases (with the exception of three isolated cases) less than $\pm 1.5\times 10^{-5}$. For the 1,200 TOA comparison cases, larger differences can be found for 27 cases that occur mostly when the viewing angle becomes large (see, e.g., results provided for 550 nm when $\theta_0 = 60°$ in **Figs. S2h** and **S2j**). Shown also in these diagrams are black error bars that denote the statistical uncertainties for *SMART-G* computations. Note that these uncertainties increase with viewing angle as discussed in Sec. 5.2.2, such that all 2,400 *SMART-G* results (i.e., including those for TOA) still remain statistically within $\pm 1.5\times 10^{-5}$ of the reflectance values listed in **Table S2**. Hence the stated uncertainty for *SMART-G* computations performed for this study is $\pm 10^{-5}$.

In **Figs. S2a–S2l** we also provide diagrams (see second and fourth row) for the relative differences $d_{\text{rel}}(R_{\text{I,Vector}})$, $d_{\text{rel}}(R_{\text{Q,Vector}})$, and $d_{\text{rel}}(R_{\text{U,Vector}})$ defined as

$$d_{\text{rel}}\left(R_{\text{I,Vector}}\right) \equiv 100 \times \left(R_{\text{I,Vector}}^{\text{Model}} - R_{\text{I,Vector}}^{\text{Table}}\right)/R_{\text{I,Vector}}^{\text{Table}}, \tag{21a}$$

$$d_{\text{rel}}\left(R_{\text{Q,Vector}}\right) \equiv 100 \times \left(R_{\text{Q,Vector}}^{\text{Model}} - R_{\text{Q,Vector}}^{\text{Table}}\right)/R_{\text{Q,Vector}}^{\text{Table}}, \tag{21b}$$

$$d_{\text{rel}}\left(R_{\text{U,Vector}}\right) \equiv 100 \times \left(R_{\text{U,Vector}}^{\text{Model}} - R_{\text{U,vector}}^{\text{Table}}\right)/R_{\text{U,Vector}}^{\text{Table}}. \tag{21c}$$

Journal Pre-proof

The yellow bars in these diagrams denote now the relative reflectance difference computed for an absolute reflectance difference of $\pm 10^{-6}$, i.e., the bars are now inversely proportional (and subsequently multiplied by 100×10^{-6}) to the magnitude of the values in **Table S2**. Note that no relative differences are shown for Stokes parameter U when $\varphi = 0°$ or $180°$ because they become then undefined (i.e. the corresponding values for U in **Table S2** become then zero). Consistent with the results shown in the first and third row of **Figs. S2a– S2l**, the relative differences for *MarCh-AD* and *SOS-CAOS* remain within the yellow error bars except for a few *SOS-CAOS* cases (see discussion above: 18 cases exhibit statistically larger differences). However the yellow error bars reveal now also that the *MarCh-AD* and *SOS-CAOS* results agree with those in **Table S2** to within $\pm 10^{-6}$ for small values (i.e., for large yellow error bars) of $R_{\mathrm{Q,Vector}}$ and $R_{\mathrm{U,Vector}}$ that occur in the vicinity to polarization minima; see, e.g., **Fig. S2d**. Except for such cases of vicinity to polarization minima, we see that the relative differences for *MarCh-AD* and *SOS-CAOS* remain well below 0.05% (and often below 0.01%). Furthermore even when these relative differences become larger, they are often caused by round-off residuals for the reflectance values reported in **Table S2** (see discussion above for absolute differences).

The relative differences $d_{\mathrm{rel}}(R_{\mathrm{I,Vector}})$, $d_{\mathrm{rel}}(R_{\mathrm{Q,Vector}})$, and $d_{\mathrm{rel}}(R_{\mathrm{U,Vector}})$ for the *SMART-G* results are displayed in the second and fourth row of **Figs. S2a–S2l**. Note that the majority of 1,200 SRF comparison cases for *SMART-G* remain within the yellow error bars. Furthermore the statistical uncertainties of *SMART-G* computations, which are denoted by black error bars in these rows, overlap with the yellow error bars for the remaining SRF comparison cases. Recall that the yellow bars correspond here to a relative reflectance difference when the absolute reflectance difference is $\pm 10^{-6}$. This implies that all 1,200 SRF comparison cases for *SMART-G* are consistent with those in **Table S2** to within $\pm 10^{-6}$. This is not true, however, for all 1,200 TOA comparison cases; see, e.g., the diagrams in **Fig. S2h** for $\theta_0 = 60°$ where the yellow and black error bars do not overlap. For those exceptions, the *SMART-G* results still remain statistically consistent with those in **Table S2** to within $\pm 1.5\times 10^{-5}$ (see discussion above for absolute differences).

Finally, **Figs. S2m** and **Fig. S2n** (see supplementary material) show the absolute difference $d_{\mathrm{abs}}(DLP)$ of the degree of linear polarization DLP for SRF and TOA, respectively. If we substitute Eqs. (19a), (19b) and (19c) for I, Q, and U in Eq. (2), respectively, we obtain

$$DLP \equiv 100 \times \frac{\sqrt{Q^2 + U^2}}{I} = 100 \times \frac{\sqrt{R^2_{\mathrm{Q,Vector}} + R^2_{\mathrm{U,vector}}}}{I}. \tag{22}$$

The absolute difference $d_{\mathrm{abs}}(DLP)$ is then obtained as follows:

$$d_{\mathrm{abs}}(DLP) \equiv DLP^{\mathrm{Model}} - DLP^{\mathrm{Tablel}} \tag{23}$$

where the first and second terms on the right-hand side of Eq. (23) are computed from the RT codes described in Secs. 4.2–4.4 and from **Table S2**, respectively. For reference, we also provide (see purple symbols and right ordinate axis) the actual values of DLP computed from **Table S2**. The yellow bars in the diagrams for $d_{\mathrm{abs}}(DLP)$ show the numerical accuracy target of 0.1% stated in Sec. 1. The black error bars are the statistical uncertainties for *SMART-G*

Journal Pre-proof

results (these uncertainties were computed from the propagation of statistical uncertainties in $R_{\mathrm{I,Vector}}$, $R_{\mathrm{Q,Vector}}$, and $R_{\mathrm{U,Vector}}$). Note that all RT code (i.e., *eGAP*, *MarCh-AD*, *SOS-CAOS*, *SMART-G*) computations for *DLP* agree within 0.1%. The agreement remains excellent even for steep gradients in *DLP* seen in the second column of **Fig. S2m** (*DLP* can change more than 20% for a 5° change in viewing angle ϑ if λ=650 nm), and for low values of *DLP* seen in the first column of **Fig. S2n** (e.g., *DLP* approaches 0.1% for λ=350 nm at ϑ = 40°). This implies that the accuracy of our RT computations for AOS model *AOS-I* is better (by a factor of 2) than the measurement accuracy for current state-of-the-art polarimeter instruments.

5.4.2 AOS-II model

The diagrams and yellow bars in **Figs. S3a–S3f** (see supplementary material) depict the same quantities as in **Figs. S2a–S2f** except for the AOS model *AOS-II* reflectance values in **Table S3**. Again, we observe that all vector RT reflectance results (i.e., 1,200 comparisons at SRF altitude for this AOS model) differ by less than 1.5×10^{-6} from one another except for one incidental *SOS-CAOS* case (see bold-face font entry for vector results in **Table S3a**) that differs from *eGAP* by 2×10^{-6}. We also observe that many differences are likely caused by round-off residuals for the values given in **Table S3** (see e.g., **Fig. S3d** where the results shown for the *MarCh-AD* and *SOS-CAOS* computations overlap one another). Finally, the relative difference in RT reflectance computations remains well below 0.05% (and often below 0.01%) except for those cases (see, e.g., again **Fig. S3d**) where the reflectance values given in **Table S3** become small. The corresponding results for the absolute RT differences in *DLP* are shown in **Fig. S3g** (see supplementary material), where we also provide the actual *DLP* values computed from **Table S3**. Here, 15 isolated cases are identified where $d_{\mathrm{abs}}(DLP)$ exceeds 0.1%. However, all these cases are likely caused by round-off residuals for the values given in **Table S3** (that is, note in **Fig. S3g** the overlap of results for the *MarCh-AD* and *SOS-CAOS* computations). Furthermore all $d_{\mathrm{abs}}(DLP)$ values remain less than 0.2%, which implies that the accuracy of our RT computations for AOS model *AOS-II* matches the measurement accuracy for current state-of-the-art polarimeter instruments.

5.4.3 AOS-III model

The RT differences for the reflectance values given in **Table S4** are shown in **Figs. S4a–S4l** (see supplementary material). The diagrams and yellow bars in these figures depict the same quantities as defined for **Figs. S2a–S2l** except for AOS model *AOS-III*. They show that the absolute RT reflectance differences for this AOS model remain less than 1.5×10^{-6} for all 2,400 comparison cases. Furthermore, most differences are likely caused by round-off residuals for the reflectance values given in **Table S4** (as evidenced by the overlapping results for the *MarCh-AD* and *SOS-CAOS* computations). The relative difference in RT reflectance computations remains again well below 0.05% (and often below 0.01%) for most scattering geometries. Furthermore, fewer scattering geometries exhibit relative reflectance differences ≥1% (which are caused by low reflectance values in **Table S4**) than for AOS models *AOS-I* and *AOS-II*. The $d_{\mathrm{abs}}(DLP)$ results for the absolute RT differences in *DLP* are shown in **Figs.**

Journal Pre-proof

S4m–S4n (see supplementary material) along with the actual values of *DLP* computed from **Table S4**. Note in these figures that all $d_{abs}(DLP)$ results remain less than 0.05% except for two cases, where $d_{abs}(DLP)$ still remains less than 0.06% and is likely caused by round-off errors (see last diagram in **Fig. S4m**). This in turn implies that our RT computations for AOS model *AOS-III* are more accurate (by a factor of 4) than the measurement accuracy for current state-of-the-art polarimeter instruments.

5.4.4 AOS-IV model

Figures S5a–S5l (see supplementary material) depict the same quantities as **Figs. S2a–S2l** except for the reflectance values for AOS model *AOS-IV* in **Table S5**. Contrary to the results for the previous AOS models, we now observe that the absolute RT reflectance difference $d_{abs}(R_{I,Vector})$ remains larger than 1.5×10^{-6} for most scattering geometries at SRF altitude. Futhermore this difference is not the result of possible round-off residuals for the reflectance values in **Table S5**. Rather, it is predominantly caused by different numerical approximations made for the large diffraction peak of particulate scattering in the ocean (see discussion in Sec. 5.2). However $d_{abs}(R_{I,Vector})$ still remains smaller than 1.5×10^{-5} for all 1,200 scattering geometries at SRF altitude except for three isolated *SOS-CAOS* cases that occur for $\vartheta \geq 50°$ at $\lambda = 550$ nm (see bold-face font entry for vector results in **Table S5b**). For those isolated cases, $d_{abs}(R_{I,Vector})$ still remains less than 2.0×10^{-5}. Furthermore, the relative RT reflectance difference $d_{rel}(R_{I,Vector})$ remains smaller than 0.05% for most scattering geometries at this altitude. The same observations can be made for the corresponding results at TOA, although both $d_{abs}(R_{I,Vector})$ and $d_{rel}(R_{I,Vector})$ become now smaller (except at $\lambda = 650$ nm). As a result, at TOA $d_{abs}(R_{I,Vector})$ reaches values between 1.5×10^{-5} and 2.0×10^{-5} for only two isolated *SOS-CAOS* cases that occur for $\vartheta \geq 55°$ at $\lambda = 550$ nm (see bold-face font entry for vector results in **Table S5d**). Note also that many of the large absolute RT reflectance differences seen at SRF altitude are still noticeable at TOA. The results for $d_{abs}(R_{Q,Vector})$ and $d_{abs}(R_{U,Vector})$ can be described in a similar manner as those for $d_{abs}(R_{I,Vector})$ except that *(i)* they remain less than 1.5×10^{-6} for many more (i.e., the majority of) scattering geometries *(ii)* there are no scattering geometries where they reach or exceed 10^{-5}. Hence the stated uncertainty for the testbed results in **Table S5** is $\pm10^{-5}$. The corresponding relative RT differences $d_{rel}(R_{Q,Vector})$ and $d_{rel}(R_{U,Vector})$ remain also smaller than 0.05% except for those scattering geometries (e.g., **Figs. S5c** and **S5f**) where $R_{Q,Vector}$ or $R_{U,Vector}$ reflectances become small in **Table S5**. Finally, **Figs. S5m– S5n** (see supplementary material) show the $d_{abs}(DLP)$ results for the absolute RT differences in *DLP*. We also provide here the actual values of *DLP* computed from **Table S5**. Note that $d_{abs}(DLP)$ remains smaller than 0.05% for all scattering geometries in spite of $d_{abs}(R_{I,Vector})$, $d_{abs}(R_{Q,Vector})$, and $d_{abs}(R_{U,Vector})$ exceeding many times 1.5×10^{-6} (but never 1.5×10^{-5} save for the above-mentioned five exception cases). We therefore conclude that our RT computations for AOS model *AOS-IV* remain more accurate (by a factor of 4) than the measurement accuracy for current state-of-the-art polarimeter instruments.

Journal Pre-proof

6. Summary

We generate and tabulate reflectance values for upwelling polarized radiance just above a wind-ruffled ocean surface and at the top of the atmosphere for a variety of scattering geometries and atmosphere-ocean systems. These tables are provided separately as supplementary material at doi:10.1016/j.jqsrt.2019.XX.XXX; see Appendix A for details. The comparison cases chosen for these results (1,200 for each altitude) capture sunglint profiles, backscattering directions, linear polarization minima profiles, and steep changes in linear polarization with viewing angle. Four atmosphere-ocean systems are chosen to focus on computations that involve *(i)* repeated reflection of light between the atmosphere and ocean surface (*AOS I* model); *(ii)* transmission of light and internal reflection by the ocean surface (*AOS II* model); *(iii)* coupling between atmospheric and oceanic scattering (*AOS III* model); and *(iv)* sharply forward-peaked scattering by marine particles (*AOS IV* model). In addition to results obtained from vector radiative transfer computations, we also provide results for scalar radiative transfer computations. All values are reported at four wavelengths that are situated in the UV (350 nm), blue (450 nm), green (550 nm), and red (650 nm) part of the spectrum. Finally, we provide reflectance values for one atmosphere-ocean system at ~370 nm to match and follow up on benchmark results that were previously published for an isolated molecular scattering slab of atmosphere.

To validate our computations, we used three independent radiative transfer codes (the *eGAP* code provided by J. Chowdhary, the *SOS-CAOS* code provided by P. Zhai, and the *MarCh-AD* code provided by F. Xu) that utilize different numerical methods (the doubling-adding method, the successive orders of scattering method, and the hybrid Markov Chain adding-doubling method) to perform multiple scattering calculations. Each code was rigorously tested for internal consistency (conservation of energy and symmetry relationships for scattering of polarized light in non-absorbing media) and checked for convergence of results in numerical approximations (by increasing the number of streams and Fourier series terms for light propagation computations). We used *eGAP* to compute all tabulated values, and *MarCh-AD* and *SOS-CAOS* to assess their associated uncertainties.

Except for some isolated cases (identified by bold-faced font entries in our tables) where the uncertainty becomes twice as large, the resulting validated accuracy of our tabulated reflectance values is 10^{-5} for the computations with sharply forward-peaked scattering by marine particles (i.e., with scattering phase functions that have asymmetry parameters ≥0.95), and it is 10^{-6} for all other computations. The corresponding relative differences in reflectance values are less than 0.05% for most cases (and often less than 0.01%), except for polarized reflectance values at scattering geometries that are in the vicinity of linear polarization minima. We also provide plots for the degree of linear polarization and show that it varies by less than 0.1% between the computations by our different radiative transfer codes for all 8,400 cases of scattering geometries, atmosphere-ocean systems, wavelengths, and altitudes considered in this work except for 15 isolated cases. The latter exceptions are caused by round-off residuals for our tabulated reflectance values, but vary still less than 0.2%. This meets our threshold objective, i.e., to provide tabulated numerical reflectance values that are more accurate than the measurement accuracy of state-of-the-art polarimetric remote sensing instruments.

Journal Pre-proof

Applicability of our tabulated reflectance values to validating probabilistic solutions of the vector radiative transfer equation is illustrated in comparisons with results obtained by a stochastic (Monte Carlo) radiative transfer code, i.e., *SMART-G* provided by D. Ramon, for the simplest atmosphere-ocean system: a molecular atmosphere above a rough ocean surface. Taking the statistical uncertainties of *SMART-G* computations into account, the agreement is within 10^{-5} at the top of the atmosphere, and within 10^{-6} just above the ocean surface, for the upwelling reflectance at all scattering geometries and wavelengths. The corresponding relative differences in reflectance values are similar to those for *SOS-CAOS* and *MarCh-AD* computations. The degree of linear polarization computed from *SMART-G* reflectance values agree within 0.1% with those computed from our tabulated reflectance values for all scattering geometries, atmosphere-ocean systems, wavelengths, and altitudes.

Appendix A: supplemental material

Supplementary tables and figures discussed in this article are given by electronic form and can be found in the online version of this article at doi:10.1016/j.jqsrt.2019.XX.XXX. The tables of supplementary material, referenced with a '**S**' preceding the table number, provide *(i)* the non-zero elements of scattering matrix $\boldsymbol{F}_p(\Theta)/(4\pi)$ for hydrosol in *AOS-IV* model; and *(ii)* reflectance testbed values $R_{I,comp}$, $R_{Q,Vector}$, $R_{U,Vector}$ for *AOS-I*, *AOS-II*, *AOS-III*, *AOS-IV*, and *AOS-I** models. The figures of supplementary material, referenced with a '**S**' preceding the figure number, provide *(i)* definitions for scattering geometries and reference plances used for the RT computations in this article; and *(ii)* absolute and relative differences between different RT code computations of reflectance testbed values $R_{I,Vector}$, $R_{Q,Vector}$, and $R_{U,Vector}$ for *AOS-I*, *AOS-II*, *AOS-III* and *AOS-IV* models.

Acknowledgements

This research was funded by the National Aeronautics and Space Administration (NASA) Ocean Biology and Biogeochemistry Program under grant number NNH13ZDA001N-PACEST, the NASA Remote Sensing of Water Quality Program under Grant Number 80NSSC18K0345, and the NASA Remote Sensing Theory Program managed by Dr. Lucia Tsaoussi.

6. References

[1] Hansen, J. E. and Travis, L. D., "Light scattering in planetary atmospheres", *Space Sci. Rev.*, **16**:527-610 (1974)

[2] Coffeen D. L. and Gehrels, T., "Wavelengths dependence of polarization, XV. Observations of Venus", *Astron. J.*, **74**:433-445 (1969)

[3] Hansen, J. E., and Hovenier, J. W., "Interpretation of the polarization of Venus", *J. Atmos. Sci.*, **31**, 1137-1160 (1974)

Journal Pre-proof

[4] Kawabata, K., Coffeen, D. L., Hansen, J. E., Lane, W. A., Sato, M. and Travis, L. D., "Cloud and haze properties from Pioneer Venus polarimetry", *J. Geophys. Res.*, **85**:8129-8140, doi:10.1029/JA085iA13p08129 (1980)

[5] Sato, M., Travis, L. D., and Kawabata, K., "Photopolarimetry analysis of the Venus atmosphere in polar regions," *Icarus,* **124**:569-585 (1996)

[6] Knibbe, W. J., de Haan, J. F., Hovenier, J. W. and Travis, L. D., "A biwavelength analysis of Pioneer Venus polarization observations", *J. Geophys. Res.*, **102**:10,945-10,957 (1997)

[7] Dollfus, A. S., Ebisawa, S., and Bowel, E., "Polarimetric analysis of the Martian dust storms and clouds in 1971", *Astron. Astrophys.*, **134**:123-136., (1984)

[8] Santer, R. M., Deschamps, M., Ksanfomality, L. V., and Dollfus, A., "Photometric analysis of the Martian atmosphere by the Soviet MARS-5 orbiter. I. White clouds and dust veils", *Astron. Astrophys.*, **150**:217-228 (1985)

[9] de Haan, J. F., "Effects of aerosols on the brightness and polarization of cloudless planetary atmospheres", PhD Thesis, Free University of Amsterdam, Enschede, The Netherlands (1987)

[10] Tomasko, G., West, R. A., and Castillo, N. D., "Photometry and polarimetry of Jupiter at large phase angles. I. Analysis of imaging data of prominent belt and a zone from Pioneer 10", *Icarus*, **33**:558-592 (1978)

[11] Carlson, B. E. and Lutz, B. L., "Time-variable Phenomena in the Jovian System", R. A. West, and J. Rahe, Eds., NASA-SP-494 (1989)

[12] Mishchenko, M. I, "The fast invariant imbedding method for polarized light: computational aspects and numerical results for Rayleigh scattering", *J. Quant. Spectrosc. Radiat. Transfer*, **43**(2):163-171 (1990)

[13] Tomasko, M. G. and Smith. P. H., "Photometry and polarimetry of Titan: Pioneer 11 observations and their implications for aerosol properties", *Icarus*, **51**, 65-95 (1982)

[14] West, R. A., Lane, A. L., Hart, H., Simmons, E., Hord, C. W., Coffeen, D. L., Esposito, L. W., Sato, M., and Pomphrey, R. B., "Voyager 2 photopolarimeter observations of Titan", *J. Geophys. Res.*, **88**:8699-8708 (1983)

[15] Bréon, F.-M., and Goloub, P., "Cloud droplet effective radius from spaceborne polarization measurements", *Geophys. Res. Lett.*, **25**:1879–1882 (1998).

[16] Herman, L., Deuzé, J.-L., Marchand, A. Roger, B and Lallart, P., "Aerosol remote sensing from POLDER/ADEOS over the ocean: Improved retrieval using a nonspherical particle model", *J. Geophys. Res.*, **110**, doi:.10.1029/2004JD004798 (2005).

[17] Waquet, F., Cornet, C., Deuzé, J.-L., Dubovik, O., Ducos, F., Goloub, P., Herman, M., Lapyonok, T., Labonnote, L. C., Riedi, J., Tanré, D., Thieuleux, F., and Vanbauce, C., "Retrieval of aerosol microphysical and optical properties above liquid clouds from POLDER/PARASOL polarization measurements", *Atmos. Meas. Tech.*, **6**:991–1016, doi:10.5194/amt-6-991-2013. (2013)

Journal Pre-proof

[18] Peers, F., Waquet, F., Cornet, C., Dubuisson, P., Ducos, F., Goloub, P., Szczap, F., Tanré, D., and Thieuleux, F., "Absorption of aerosols above clouds from POLDER/PARASOL measurements and estimation of their direct radiative effect", *Atmos. Chem. Phys*., **15**:4179–4196, doi:10.5194/acp-15-4179-2015 (2015)

[19] Loisel, H., Duforet, L., Dessailly, D., Chami, M., and Dubuisson, P., "Investigation of the variations in the water leaving polarized reflectance from the POLDER satellite data over two biochemical contrasted oceanic areas", *Opt. Express*, **16**(17):12905-12918 (2008)

[20] Ibrahim, A., Gilerson, A., Chowdhary, J., and Ahmed, S., "Retrieval of macro- and micro-physical properties of oceanic hydrosols from polarimetric observations", *Remote Sens. of Environ.*, **186**:548-566 (2016)

[21] He, X., Delu , D., Bai, Y., Wang, D. and Zengzhou Hao, Z., "A new simple concept for ocean colour remote sensing using parallel polarisation radiance", *Scientific Reports*, **4**, Article number: 3748, doi:10.1038/srep03748 (2014)

[22] Cairns, B., Russell, E. E., and Travis, L. D., "The research scanning polarimeter: calibration and ground-based measurements", *Proceedings of SPIE*, **3754**:186-197 (1999)

[23] van Harten, G., Snik, F., Rietjens, J. H. H., Smit, J. M., de Boer, J. , Diamantopoulou, R., Hasekamp, O. P. , Stam, D. M., Keller, C. U., Laan, E. C., Verlaan, A. L.,. Vliegenthart, W. A., ter Horst, R. , Navarro, R., Wielinga, K. , Hannemann, S. , Moon, S. G., Voors, R., "Prototyping for the Spectropolarimeter for Planetary EXploration (SPEX): calibration and sky measurements", *Proc. SPIE 8160, Polarization Science and Remote Sensing V*, 81600Z, doi: 10.1117/12.893741 (2011)

[24] van Harten, G., Diner, D. J., Daugherty, B. J. S., Rheingans, B. E., Bull, M. A., Seidel, F. C., Chipman, R. A., Cairns, B., Wasilewski, A. P., and Knobelspiesse, K. D., "Calibration and validation of Airborne Multiangle SpectroPolarimetric Imager (AirMSPI) polarization measurements", *Appl. Opt.*, **57**(16):4499-4513 https://doi.org/10.1364/AO.57.004499 (2018)

[25] Diner, D. J., Xu, F., Garay, M. J., Martonchik, J. V., Rheingans, B. E., Geier, S., Davis, A., Hancock, B. R., Jovanovic, V. M., Bull, M. A., Capraro, K., Chipman, R. A., and McClain, S. C., "The Airborne Multiangle SpectroPolarimetric Imager (AirMSPI): a new tool for aerosol and cloud remote sensing", *Atmos. Meas. Tech.*, **6**:2007-2025, https://doi.org/10.5194/amt-6-2007-2013 (2013)

[26] Mishchenko, M. I. and Travis, L. D., "Satellite retrieval of aerosol properties over the ocean using measurements of reflected sunlight: effect of instrumental errors and aerosol absorption", *J. Geophys. Res*., **102**:13,543-13,553 (1997a)

[27] Knobelspiesse, K., Cairns, B., Mishchenko, M., Chowdhary, J., Tsigaridid, K., van Diedenhoven, B., Martin, W., Ottaviani, M., and Alexandrov, M., "Analyses of fine-mode aerosol retrieval capabilities by different passive remote sensing instrument designs", *Opt. Express*, **20**(19):21457-21484 (2012)

[28] Mishchenko, M. I., Cairns, B., Kopp, G., Schueler, C. F., Fafaul, B. A., Hansen, J. E., Hooker, R. J., Itchkawich, T., Maring, H. B., and Travis, L. D., "Accurate monitoring

Journal Pre-proof

of terrestrial aerosols and total solar irradiance: introducing the Glory Mission", *Bull. Amer. Meteor. Soc,*, **88**:677−691 (2007).

[29] Hasekamp, O. P., Fu, G., Rusli, S. P., Wu, L., Di Noia, A., Brugh, J. aan de, Landgraf, J., Smit, J. M., Rietjes, J. Amerongen, A. van, "Aerosol Measurements by SPEXone on the NASA PACE Mission: expected retrieval capabilities", *J. Quant. Spectrosc. Radiat. Transfer*, **227**:170–184, https://doi.org/10.1016/j.jqsrt.2019.02.006, (2019)

[30] Ottaviani, M., Chowdhary, J., and Cairns, B., "Remote sensing of the ocean surface refractive index via short-wave infrared polarimetry", *Remote Sens. of Environ.*, **221**:14-23 (2019)

[31] NASA, "PACE Science Definition Team Report", 308 pp, https://pace.oceansciences.org/docs/PACE_TM2018-219027_Vol_2.pdf (2018a)

[32] NASA, "Polarimetry in the PACE mission: Science Team Consensus Document", PACE Technical Report Series, Vol. 3, NASA/TM–2018-219027/ Vol. 3, 32 pp, https://pace.oceansciences.org/docs/TM2018219027Vol.3.pdf (2018b)

[33] Werdell, J. P., Behrenfeld, M. J., Bontempi, P. S., Boss, E., Cairns, B., Davis, G. T., Gliese, U. B., Gorman, E. T., Hasekamp, O., Knobelspiesse, K. D., Mannino, A., Martins, J. V., McClain, C. R., Meister, G., and Remer, L. A., "The Plankton, Aerosol, Cloud, ocean Ecosystem (PACE) mission: status, science, advances", *Bull. Amer. Meteor. Soc,*, doi 10.1175/BAMS-D-18-0056.1 (2019)

[34] Coulson, K. L., Dave, J. V., and Sekera, Z.,"Tables related to radiation emerging from a planetary atmosphere with Rayleigh scattering", University of California Press (1960)

[35] Stammes P., de Haan J. F., and Hovenier J. W., "The polarized internal radiation field of a planetary atmosphere", *Astron. Astroph.*, **225**:239-259 (1989)

[36] Natraj, V., Li, K.-F., and Yung, Y. L., "Rayleigh scattering in planetary atmospheres: corrected tables through accurate computation of X and Y functions", *Astrophys. J.*, **691**:1909-1920, doi:10.1088/0004-637X/691/2/1909 (2009)

[37] Natraj, V. and Hovenier, J. W., "Polarized light reflected and transmitted by thick Rayleigh scattering atmospheres", *Astrophys. J.*, **748**:28, doi:10.1088/0004-637X/748/1/28 (2012)

[38] de Haan, J. F., Bosma, P. B., and Hovenier, J. W., "The adding method for multiple scattering computations of polarized light", *Astron. Astrophys.*, **183**:371-391 (1987)

[39] Siewert, C. E., "A discrete-ordinates solution for radiative-transfer models that include polarization effects", *J. Quant. Spectrosc. Radiat. Transfer*, **64**:227-254 (2000)

[40] Kokhanovsky, A. A., Budak, V. P., Cornet, C., Duan, M., Emde, C., Katsev, I. L., Klyukov, D. A., Korkin, S. V., Labonnote, L. C., Mayer, B., Min, Q , Nakajima, T., Ota, Y., Prikhach, A. S., Rozanov, V. V., Yokota, T., Zege, E. P., "Benchmark results in vector atmospheric radiative transfer", *J. Quant. Spectrosc. Radiat. Transfer*, **111**(12–13):1931-1946, ISSN 0022-4073, http://dx.doi.org/10.1016/j.jqsrt.2010.03.005 (2010)

[41] Escribano, J., Bozzo, A., Dubuisson, P., Flemming, J., Hogan, R. J., Labonnote, L. C.-, and Boucher, O., "A benchmark for testing the accuracy and computational cost of shortwave top-of-atmosphere reflectance calculations in clear-sky aerosol-loaden atmospheres", *Geosci. Model Dev.*, **12**(2):805-827 (2019)

Journal Pre-proof

[42] Zhai, P.-W., Hu, Y., Chowdhary, J., Trepte, C. R., Lucker, P. L., Josset, D. B., "A vector radiative transfer model for coupled atmosphere and ocean systems with a rough interface", *J. Quant. Spectrosc. Radiat. Transfer*, **111**(7–8): 1025-1040, ISSN 0022-4073, http://dx.doi.org/10.1016/j.jqsrt.2009.12.005. (2010)

[43] Hollstein, A., and Fischer, J. "Radiative transfer solutions for coupled atmosphere ocean systems using the matrix operator technique", *J. Quant. Spectrosc. Radiat. Transfer*, **113**:536-548, doi:10.1016/j.jqsrt.2012.01.010 (2012)

[44] Cohen, D., Stamnes, S., Tanikawa, T., Sommersten, E. R., Stamnes, J. J., Lotsberg, J. K., and Stamnes, K., "Comparison of discrete ordinate and Monte Carlo simulations of polarized radiative transfer in two coupled slabs with different refractive indices', *Opt. Express*, **21(8)**, doi:10.1364/OE21.009592 (2013)

[45] Chami, M., Lafrance, B., Fougnie, B., Chowdhary, J., Harmel, T., and Waquet, F., "OSOAA: a vector radiative transfer model of coupled atmosphere-ocean system for a rough sea surface application to the estimates of the directional variations of the water leaving reflectance to better process multi-angular satellite sensors data over the ocean", *Opt. Express*, **23**(21): DOI:10.1364/OE.23.027829 (2015)

[46] Emde, C., Barlakas, V., Cornet, C., Evans, F., Korkin, S., Ota, Y., Labonnote, L. C., Lyapustin, A., Macke, A., Mayer, B., Wendisch, M., "IPRT polarized radiative transfer model comparison project – Phase A", *J. Quant. Spectrosc. Radiat. Transfer*, **164**:8-36 (2015)

[47] Mobley, C. D., Gentili, B., Gordon, H. R., Jin, Z., Kattawar, G. W., Morel, A., Reinersman, P., Stamnes, K., and Stavn, R., "Comparison of numerical models for computing underwater light fields", *Appl. Opt.*, **32**(36):7484-7504 (1993)

[48] Bulgarelli, B. and Doyle, J. P., "Comparison between numerical models for radiative transfer simulation in the atmosphere-ocean system", *J. Quant. Spectrosc. Radiat. Transfer*, **86**:315-334, https://doi.org/10.1016/j.jqsrt.2003.08.009 (2004)

[49] Chowdhary, J., Zhai, P.-W., Boss, E., Dierssen, H., Frouin, R., Ibrahim, A., Lee, Z., Remer, L. A., Twardowski, M., Xu, F., Zhang, X., Ottaviani, M., Espinosa, W. R., and Ramon, D., "Modeling atmosphere-ocean radiative transfer: A PACE mission perspective", *Front. Earth Sci*., doi: 10.3389/feart.2019.00100 (2019)

[50] Frouin, R., Franz, B., Ibrahim, A., Ahmad, Z., Cairns, B., Chowdhary, J., Dierssen, H. M., Tan, J., Dubovik, O., Huang, X., Davis, A. B., Kalashnikova, O., Thompson, D. R., Remer, L. A., Boss, E., Coddington, O., Deschamps, P.-Y., Gao, B.-C., Gross, L., Hasekamp, O., Omar, A., Pelletier, B., Ramon, D., Steinmetz, F., and Zhai, P.-W., "Atmospheric correction of satellite ocean-colorimagery during the PACE era", *Front. Earth Sci*., doi: 10.3389/feart.2019.00145 (2019)

[51] Remer, L. A., Knobelspiesse, K., Zhai, P.-W., Xu, F., Kalashnikova, O., Chowdhary, J., Hasekamp, O., Dubovik, O., Wu, L., Ahmad, Z., Boss, E., Cairns, B., Coddington, O., Davis, A. B., Dierssen, H. M., Diner, D. J., Franz, B., Frouin, R., Gao, B.-C., Ibrahim, A., Levy, R. C., Omar, A. H., and Torres, O., "Retrieving aerosol characteristics from the PACE mission. Part 2: Multi-angle and polarimetry, *Front. Environ. Sci*., doi: 10.3389/fenvs.2019.00094 (2019).

[52] Kawata, Y., and Yamazaki, A., "Multiple scattering analysis of airborne POLDER

Journal Pre-proof

image data over the sea", *IEEE Trans. Geosci. Remote Sens.*, **51**:51−60 (1998).

[53] Adams, J. T. and Kattawar, G. W, "Neutral points in an atmosphere–ocean system. 1: Upwelling light field", *Appl. Opt.*, **36**:1976-1986 (1997)

[54] Chowdhary, J., Cairns, B., Waquet, F., Knobelspiesse, K., Ottaviani, M., Redemann, J., Travis, L., and Mishchenko, M., "Sensitivity of multiangle, multispectral polarimetric remote sensing over open oceans to water-leaving radiance: Analyses of RSP data acquired during the MILAGRO campaign", *Remote Sens. of Environ.*, **118**:284-308 (2012)

[55] Hovenier, J. W. and van der Mee C. V. M., "Fundamental relationships relevant to the transfer of polarized light in a scattering atmosphere", *Astron. Astrophys.*, **128**:1-16 (1983).

[56] van de Hulst, H. C., "Light Scattering by Small Particles", 470 pp, John Wiley, New York (1957)

[57] Twardowski, M., Claustre, H., Freeman, S. A., Stramski, D., Huot, Y., "Optical backscattering properties of the "clearest" natural waters", *Biogeosciences Discuss.*, **4**(4):2441-2491 (2007)

[58] Zhang, X, Hu, L., and He, M.-X., "Scattering by pure sea water: Effects of salinity", *Opt. Express*, **17** (7):5698 (2009)

[59] Smith, R. C., and Baker, K. S., "Optical properties of the clearest natural waters (200-800 nm)", *Appl. Opt.*, **20**(2):177-184 (1981)

[60] Farinato, R. S. and Rowell, R. L., "New values of the light scattering depolarization and anisotropy of water", *J. Chem. Phys.*, **65**:593-595 (1976).

[61] Zhang, X., and Hu, L., "Estimating scattering of pure water from density fluctuation of the refractive index", *Opt. Express*, **17**:1671-1678 (2009).

[62] Zhang, X., Stramski, D., Reynolds, R. A., and Blocker, E. R., "Light scattering by pure water and seawater: the depolarization ratio and its variation with salinity", *Appl. Opt.*, **58**:991-1004 (2019)

[63] Buiteveld, H., Hakvoort, J. H. M. and Donze, M., "The optical properties of pure water", *SPIE Ocean Optics XII*, **2258**:174–183, (1994)

[64] Morel, A.," Optical properties of pure water and pure sea water", in *Optical Aspects of Oceanography*, edited by N. G. Jerlov, and Nielsen, E. S., pp. 1-24, Academic, New York (1974)

[65] Shifrin, K. S., "Physical optics of ocean water", Springer Science & Business Media (1988)

[66] Chowdhary, J. Cairns, B., and Travis, L. D., "Contribution of water-leaving radiance to multiangle, multispectral polarimetric observations over the open ocean: bio-optical model results for case 1 waters", *Appl. Opt.*, **45**(22):5542-5587 (2006)

[67] Morel, M and Maritorena, S., "Bio-optical properties of oceanic waters: A reappraisal", *J. Geophys. Res.*, **106**(C4):7163-7180 (2001)

[68] Whitmire, A. L., Boss, E., Cowles, T. J., and Pegau, W. S., "Spectral variability of the particle backscatter ratio", *Opt. Express*, **15**(11):7019:7031 (2007)

Journal Pre-proof

[69] Huot, Y., Morel, A., Twardowski, M. S., Stramski, D., and Reynolds, R. A., "Particle optical backscattering along a chlorophyll gradient in the upper layer of the eastern South Pacific Ocean", *Biogeosciences*, **5**:495–507 (2008)

[70] McKee, D. and Cunningham, A., "Evidence for wavelength dependence of the scattering phase function and its implication for modeling radiance transfer in shelf seas", *Appl. Opt.*, **44**:126-135 (2005)

[71] Chami, M., Shybanov, E. B., Khomenko, G. A., M. E.-G. Lee, M. E.-G., Martynov, O. V. and G. K. Korotaev, G. K., "Spectral variation of the volume scattering function measured over the full range of scattering angles in a coastal environment", *Appl. Opt.*, **45**:3605-3619 (2006)

[72] Kitchen, J. K. and Zaneveld, J. R. V., "A three-layered sphere model of the optical properties of phytoplankton", *Limnol. Oceanogr.*, **37**(8):1680-1690 (1992)

[73] Quirantes, A. and Benard, S. "Light scattering by marine algae: two-layer spherical and nonspherical models", *J. Quant. Spectrosc. Radiat. Transfer*, **89**:311–321 (2004).

[74] Organelli, E., Dall'Olmo, G., Brewin, R. J. W., Tarran, G. A., Boss, E., and Bricaud, A., "The open-ocean missing structural complexity of particles", *Nature Communications*, **9**:5439, https://doi.org/10.1038/s41467-018-07814-6 (2018)

[75] Gordon, H.R., "Backscattering of light from disk like particles: is fine-scale structure or gross morphology more important?", *Appl. Opt.*, **45**:7166–7173 (2006).

[76] Clavano, W. R., Boss, E., and Karp-Boss, L., "Inherent optical properties of non-spherical marine-like particles – from theory to observations", *Oceanography and Marine Biology: An Annual review*, **45**:1-45 (2007)

[77] Poulin, C., Zhang, X., Yang, P., and Huot, Y., "Diel variations of the attenuation, backscattering and absorption coefficients of four phytoplankton species and comparison with spherical, coated spherical and hexahedral particle optical models", *J. Quant. Spectrosc. Radiat. Transfer*, **217**:288-305 (2018)

[78] Pope, R. and Fry, E., "Absorption spectrum (380 - 700 nm) of pure waters: II. Integrating cavity measurements", *Appl. Opt.*, **36**:8710-8723 (1997)

[79] Sogandares, F. M. and Fry, E. S., "Absorption spectrum (340–640 nm) of pure water. I. Photothermal measurements", *Appl. Opt.*, **36**:8699-8709 (1997)

[80] Pegau, W. S., Gray, D. and Zaneveld, J. R. V., "Absorption and attenuation of visible and near-infrared light in water: dependence on temperature and salinity", *Appl. Opt.*, **36**(24):6035-6046 (1997)

[81] Sullivan, J. M., Twardowski, M. S., Zaneveld, J. R. V., Moore, C. M., Barnard, A. H., Donaghay, P. L., and Rhoades, B.,"Hyperspectral temperature and salt dependencies of absorption by water and heavy water in the 400-750 nm spectral range", *Appl. Opt.*, **45**(21):5294–5309 (2006).

[82] Röttgers, R., McKee, D., and Utschig, C., "Temperature and salinity correction coefficients for light absorption by water in the visible to infrared spectral region", *Opt. Express*, **2** (21), DOI:10.1364/OE.22.025093 (2014)

Journal Pre-proof

[83] Morel, A., Claustre, D., and Gentili, B., "Natural variability of bio-optical properties in Case 1 waters: attenuation and reflectance within the visible and near-UV spectral domains, as observed in South Pacific and Mediterranean waters", *Biogeosciences*, **4**:913-925 (2007)

[84] Cox, C. and Munk, W., "Measurement of the Roughness of the Sea Surface from Photographs of the Sun's Glitter", *J. Opt. Soc. Am.*, **44**:838-850 (1954)

[85] Masuda, K., "Effects of the speed and direction of surface winds on the radiation in the atmosphere-ocean system", *Remote Sens. of Environ.*, **64**:53-63 (1998)

[86] Sancer, M. I., "Shadow-corrected electromagnetic scattering from a randomly rough surface", *IEEE Trans. Ant. Prop.*, **17**:577–585 (1969).

[87] Preisendorfer, R. W. and Mobley, C. D., "Albedos and glitter patterns of a wind-roughened sea surface", *J. Phys. Oceanogr.*, **16**:1293-- (1986)

[88] Mobley, C. D., "Polarized reflectance and transmittance properties of windblown sea surface", *Appl. Opt.*, **54**(15):4828-4849 (2015)

[89] Koepke, P., "Effective reflectance of oceanic whitecaps", *Appl. Opt.*, **23**:1816-- (1984)

[90] Frouin, R., Schwindling, M., and Deschamps, P. –Y, "Spectral reflectance of sea foam in the visible and near-infrared: in situ measurements and remote sensing applications", *J. Geophys. Res.*, **101**:14,361-14,371 (1996)

[91] Moore, K. D., Voss, K. J., and Gordon, H. R., "Spectral reflectance of whitecaps: Their contribution to water-leaving radiance", *J. Geophys. Res.*, **105**(C3):6493-6499 (2000)

[92] Kokhanovsky, A. A., "Spectral reflectance of whitecaps", *J. Geophys. Res.: Oceans*, **109**, doi:10.1029/2003JC002177 (2004)

[93] Dierssen, H. M., "Hyperspectral measurements, parameterizations, and atmospheric correction of whitecaps and foam from visible to shortwave infrared for ocean color remote sensing", *Front. Earth Sci.*, **7**:14. doi: 10.3389/feart.2019.00014 (2019)

[94] Chowdhary, J., "Multiple scattering of polarized light in atmosphere-ocean systems", Ph D Thesis, Columbia University, New York (1999).

[95] Bodhaine, B. A., Wood, N. B., Dutton, E. G., Slusser, J. R., "On Rayleigh Optical Depth Calculations", *J. Atmos. Oceanic Technol.*, **16**:1854–1861 (1999)

[96] Orphane, J., and Chance, K., "Ultraviolet and visible absorption cross-sections for HITRAN", *J. Quant. Spectrosc. Radiat. Transfer*, **82**: 491-504 (2003)

[97] Ibrahim, A., Franz, B., Ahmad, Z., Haly, R., Knobelspiesse, K., Gao, Bo-Cai, Proctor, C., and Zhai, P. W., "Atmospheric correction for hyperspectral ocean color retrieval with application to the Hyperspectral Imager for the Coastal Ocean (HICO)", *Remote Sens. of Environ.*, **204**:60-75, http://dx.doi.org/10.1016/j.rse.2017.10.041 (2018)

[98] Dubovik, O., Sinyuk, A., Lapyonok, T., Holben, B. N., Mishchenko, M., Yang, P., Eck, T. F., Volten, H., Muñoz, O., Veihelman, B., van der Zande, W. J., Leon, J,-F., Sorokin, M., & Slutsker, I., "Application of spheroid models to account for aerosol particle nonsphericity in remote sensing of desert dust", *J. Geophys. Res.*, **111**, D11208 doi:10.1029/2005JD006619 (2006).

Journal Pre-proof

[99] Yang, P., Feng, Q., Hong, G , Kattawar, G. W., Wiscombe, W. J., Mishchenko, M. I., Dubovik, O., Laszlo, I. and Sokolik, I. N., "Modeling of the scattering and radiative properties of nonspherical dust-like aerosols", *J. Aerosol Sci.*, **38**(10): 995–1014, doi:10.1016/j.jaerosci.2007.07.001 (2007),

[100] Voss, K. J. and Fry, E. S., "Measurements of the Mueller matrix for ocean water", *Appl. Opt.*, **23**:4427-4439 (1984)

[101] Quinby-Hunt, M. S., Hunt, A. J., Lofftus, K., and Shapiro, D., "Polarized-light scattering studies of marine Chlorella", *Limnol. Oceanogr.*, **34**(8):1587-1600 (1989)

[102] Volten, H., de Haan, J. F., Hovenier, J. W., Schreurs, R., Vassen, W., Dekker, A. G., Hoogenboom, H. J., and Charlton, F., "Laboratory measurements of angular distributions of light scattering by phytoplankton and silt", *Limnol. Oceanogr.*, **43**:1180-1197 (1998)

[103] Hovenier, J. W., "Symmetry relationships for scattering of polarized light in a slab of randomly oriented particles", *J. Atm. Sci.*, **26**:488-499 (1969).

[104] Nakajima, T. and Tanaka, M., "Effect of wind-generated waves on the transfer of solar radiation in the atmosphere-ocean system", *J. Quant. Spectrosc. Radiat. Transfer*, **29**:521-- (1983)

[105] Mishchenko, M. I., Dlugach, J. M., Chowdhary, J., and Zakharova, N. T., "Polarized bidirectional reflectance of optically thick radiance: An efficient numerically exact radiative transfer solution", *J. Quant. Spectrosc. Radiat. Transfer*, **156**:97-108, doi:10.1016/j.jqsrt.2015.02.003 (2015)

[106] Xu, F., Dubovik, O., Zhai, P.-W., Diner, D. J., Kalashnikova, O. V., Seidel, F. C., Litvinov, P., Bovchaliuk, A., Garay, M. J., van Harten, G., and Davis, A. B., "Joint retrieval of aerosol and water-leaving radiance from multispectral, multiangular and polarimetric measurements over ocean", *Atmos. Meas. Tech.*, **9**:2877-2907, 2016.

[107] Esposito, L.W. and House L. L., "Radiative transfer calculated by a Markov chain formalism", *Astrophys. J.*, **219**:1058–1067 (1978).

[108] Xu, F., Davis, A.B., West, R.A., and Esposito, L.W., "Markov chain formalism for polarized light transfer in plane-parallel atmospheres, with numerical comparison to the Monte Carlo method", *Opt. Express*, **19**:946-967 (2011a)

[109] Xu, F., Davis, A.B., West, R.A., Martonchik, J.V., and Diner, D.J., "Markov chain formalism for vector radiative transfer in a plane-parallel atmosphere overlying a polarizing surface", *Opt. Lett.*, **36**:2083-2085 (2011b).

[110] Esposito, L.W. "An 'adding' algorithm for the Markov chain formalism for radiation transfer", *Astrophys. J.*, **233**:661–663 (1979).

[111] Smith, B. G., "Geometrical shadowing of a random rough surface", *IEEE Trans. Ant. Prop.*, **15**:668–671 (1967).

[112] Zhai, P.-W., Hu, Y., Trepte, C. R., and Lucker, P. L., "A vector radiative transfer model for coupled atmosphere and ocean systems based on successive order of scattering method", *Opt. Express*, **17**:2057-2079 (2009)

[113] Wiscombe, W. J., "The Delta-M method: rapid yet accurate radiative flux calculations for strongly asymmetric phase functions", *J. Atmos. Sci.*, **34**:1408–1422 (1977).

Journal Pre-proof

[114] Hu, Y., Wielicki, B., Lin, B., Gibson, G., Tsay, S.-C, Stamnes, K., Wong, T., "δ-Fit: A fast and accurate treatment of particle scattering phase functions with weighted singular-value decomposition least-squares fitting", *J. Quant. Spectrosc. Radiat. Transfer*, **65**(4):681-690, ISSN 0022-4073, http://dx.doi.org/10.1016/S0022-4073(99)00147-8 (2000)

[115] Zhai; P.-W., Hu, Y., Josset, D. B., Trepte, C. R., Lucker, P. L., Lin, B., "Exact first order scattering correction for vector radiative transfer in coupled atmosphere and ocean systems", Proc. *SPIE 8364, Polarization: Measurement, Analysis, and Remote Sensing X*, **83640A**, doi:10.1117/12.920767 (2012)

[116] Schulz, F.M., and Stamnes, K., "Angular distribution of the Stokes vector in a plane-parallel, vertically inhomogeneous medium in the vector discrete ordinate radiative transfer (VDISORT) model", *J. Quant. Spectrosc. Radiat. Transfer*, **65**(4): 609-620, ISSN 0022-4073, http://dx.doi.org/10.1016/S0022-4073(99)00115-6 (2000)

[117] Zhai, P.-W., Hu, Y., Josset, D. B., Trepte, C. R., Lucker, P. L., Lin, B., "Advanced angular interpolation in the vector radiative transfer for coupled atmosphere and ocean systems", *J. Quant. Spectrosc. Radiat. Transfer*, **115**:19-27, ISSN 0022-4073, http://dx.doi.org/10.1016/j.jqsrt.2012.09.018 (2013)

[118] Rahman, H., Pinty, B., and Verstraete, M. M., "Coupled surface-atmosphere reflectance (CSAR) model: 2. Semiempirical surface model usable with NOAA advanced very high resolution radiometer data", *J. Geophys. Res.*, **98**(D11), 20791–20801, doi:10.1029/93JD02072 (1993)

[119] Martonchik, J. V., Diner, D. J., Pinty, B., Verstraete, M. M. , Myneni, R. B., Knyazikhin, Y., and Gordon, H. R., "Determination of land and ocean reflective, radiative, and biophysical properties using multiangle imaging", *IEEE Trans. Geosci. Remote Sens.*, **40** (4):1266-1281 (1988)

[120] Zhai, P.-W., Hu, Y., Winker, D. M., Franz, B. A., and Boss, E., "Contribution of Raman scattering to polarized radiation field in ocean waters", *Opt. Express*, **23**:23582-23596 (2015)

[121] Zhai P., Hu, Y., Winker, D. M., Franz, B., Werdell, J., Boss, E., "A vector radiative transfer model for coupled atmosphere and ocean systems including inelastic sources in ocean waters", *Opt. Express*, **25**:A223-A239 (2017)

[122] Zhai, P., Boss, E., Franz, B., Werdell, P. J., Hu, Y., "Radiative transfer modeling of phytoplankton fluorescence quenching processes", *Remote Sens.*, **10**(8), 1309 (2018).

[123] Zhai, P.-W., Kattawar, G. W., and Yang,, P., "Impulse response solution to the three-dimensional vector radiative transfer equation in atmosphere-ocean systems. I. Monte Carlo method", *Appl. Opt.*, **47**:1037-1047 (2008)

[124] Ramon, D., Steinmetz, F., Jolivet, D., Compiègne, M. and Frouin, R. "Modelling polarized radiative transfer in the ocean-atmosphere system with the GPU-accelerated SMART-G Monte Carlo code", *J. Quant. Spectrosc. Radiat. Transfer*, **222-223**:89-107 (2019)

[125] Mayer, B., "Radiative transfer in the cloudy atmosphere", *Eur. Phys. J. Conferences*, **1**:75-99, doi: 10.1140/epjconf/e2009-00912-1 (2009)

[126] Plass, G. N., Kattawar, G. W., Guinn, J. A. Jr., "Radiative transfer in the Earth's atmosphere and ocean: influence of ocean waves", *Appl. Opt.*, **14**:1924–36. doi: 10.1364/AO.14.001924 (1975).

Journal Pre-proof

[127] Ross, V., Dion, D., and b, G., "Detailed analytical approach to the Gaussian surface bidirectional reflectance distribution function specular component applied to the sea surface", *J. Opt. Soc. Am. A*, **22**:2442–2453 (2005).

[128] Mishchenko, M. I., Travis. L. D., "Satellite retrieval of aerosol properties over the ocean using and polarization as well as intensity of reflected sunlight", *J. Geophys. Res.*, **102**:16,989–17,013 (1997b)

[129] Marchuk, G. I., Mikhailov, G. A., Nazaraliev, M. A., "The Monte Carlo methods in atmo- spheric optics", Berlin Heidelberg, Springer-Verlag (1980)

[130] Buras, R., and Mayer. B., "Efficient unbiased variance reduction techniques for Monte Carlo simulations of radiative transfer in cloudy atmospheres: the solution", *J. Quant. Spectrosc. Radiat. Transf.*, **112**:434–447 (2011).

[131] Potter, J. F., "The delta function approximation in radiative transfer theory", *J. Atmos. Sci.*, **27**:943–949 (1970)

[132] Hovenier, J. W. and de Haan, J. F., "Polarized light in planetary atmospheres for perpendicular directions", *Astron. Astrophys.*, **146**:185–191 (1985).

`

Journal Pre-proof

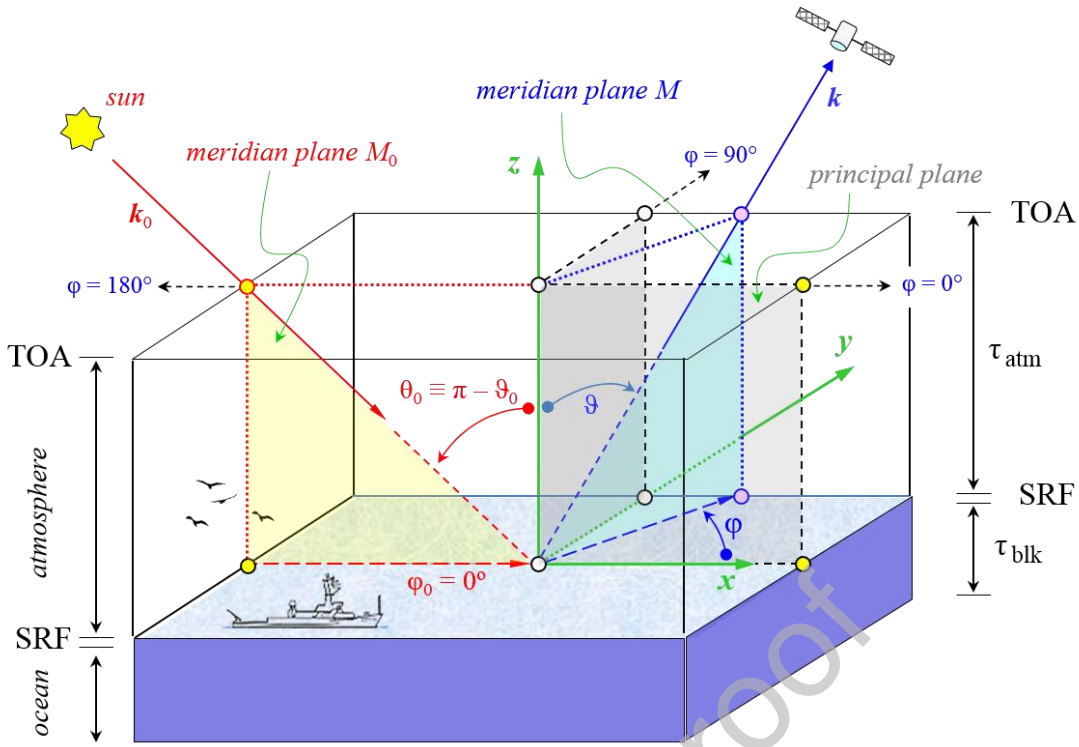

Figure 1. Conventions used in this work for scattering geometries and for reference planes in RT computations for atmosphere-ocean systems. Note that meridian plane M_0 coincides with the solar principal plane.

Print instructions: **2-column fitting image**
color reproduction in print

Table 1. Overview and references for AOS models used in this study.

AOS model	*Ocean Body*	*Ocean Surface*	*Atmosphere*
AOS-I, *AOS-I** §	*none*	rough‡ • see *Sec. 3.2* • see **Table 4**	molecular† • see *Sec. 3.3* • see **Table 5a**, **5b**
AOS-II	pure water† • see *Sec. 3.1* • see **Table 2**	rough‡ • see *Sec. 3.2* • see **Table 4**	*none*
AOS-III	pure water† • see *Sec. 3.1* • see **Table 2**	rough‡ • see *Sec. 3.2* • see **Table 4**	molecular† • see *Sec. 3.3* • see **Table 5a**
AOS-IV	pure water† & hydrosol • see *Sec. 3.1* • see **Table 2** & **3**, **S1**	rough‡ • see *Sec. 3.2* • see **Table 4**	molecular† • see *Sec. 3.3* • see **Table 5a**

§ *AOS-I* and *AOS-I** models differ in sun & viewing geometries and in atmospheric optical depth
† Rayleigh scattering with zero depolarization
‡ no shadowing effects, no ocean foam, no renormalization

Journal Pre-proof

Table 2. Ocean body scattering coefficients b_w and b_p, absorption coefficients a_w and a_{blk}, single scattering albedos ω_{blk}, and optical thicknesses τ_{blk}, for *AOS-II* to *AOS-IV* models

AOS model	*Property*	*Equation*	[Chl] = 0.03 mg/m^3		[Chl] = 3.00 mg/m^3	
			λ = 350 nm	λ = 450 nm	λ = 550 nm	λ = 650 nm
II, III, IV	$b_w(\lambda)$ §	(3), (10), (12)	0.0134	0.0045	0.0019	0.0010
II, III	$b_p(\lambda)$	(3), (10), (12)	0	0	0	0
	$a_{blk}(\lambda)$	(11a)	0.0204	0.0092	0.0565	0.3400
	$\omega_{blk}(\lambda)$	(10)	0.39644970	0.32846715	0.03253425	0.002932551
	$\tau_{blk}(\lambda)$ †	(12)	3.38	1.37	5.84	34.1
IV	$b_p(\lambda,[Chl])$	(3), (10), (12)	0.0422	0.0335	0.8050	0.8050
	$a_{blk}(\lambda,[Chl])$	(11b)	0.0215	0.0144	0.1065	0.3787
	$\omega_{blk}(\lambda,[Chl])$	(10)	0.72114137	0.72519084	0.88340267	0.68034101
	$\tau_{blk}(\lambda,[Chl])$ †	(12)	7.71	5. 24	91.34	118.47

§ Does not vary with [Chl]; † For Δz_{ocean} = 100 m

Table 3. Properties and mixing ratios of D-P hydrosol components (i.e. of detritus and phytoplankton mixtures) for *AOS-IV* model.

AOS model	*Property*	*Equation*	Detritus	Phytoplankton
IV	Junge size distribution exponent γ §	-	γ_{dm} = 4.4	γ_{ph} = 3.7
	Refractive index m	-	m_{dm} = 1.15	m_{ph} = 1.04
	Backscattering ratio $\tilde{b}_b$	(7)	$\tilde{b}_{b,dm}$ = 4.444×10^{-2}	$\tilde{b}_{b,ph}$ = 2.663×10^{-3}
	Scattering cross section σ †	(9)	σ_{dm} = 1.388×10^{-5}	σ_{ph} = 8.874×10^{-5}
	Mix ratio f for [Chl] = 0.03 mg/m^3 a)	(9)	f_{dm} = 0.61	f_{ph} = 1 – f_{dm}
	Mix ratio f for [Chl] = 3.00 mg/m^3 b)	(9)	f_{dm} = 0.34	f_{ph} = 1 – f_{dm}

§ Assuming spherical particles with radii between 0.01 – 100 µm; † in µm^2, computed at λ = 550 nm and assumed spectrally invariant

a) mixture $\tilde{b}_{b,p}$ = 0.0108; b) mixture $\tilde{b}_{b,p}$ = 0.0058

Table 4. Ocean surface properties.

AOS model	*Surface Model*	*Roughness*	*Equation*	χ^2	m_w
I, I, II, III, IV*	*Cox and Munk* (1954)	*Gaussian isotropic* §	(13), (14)	0.03884 ‡	1.34 – 0*i*

§ No shadowing effects, no ocean foam, no normalization

‡ This corresponds to $W \approx 7$ m/s

Journal Pre-proof

Table 5a. Single scattering albedo ω_{mol} and extinction optical thicknesses τ_{mol} for the atmosphere in *AOS-I* to *AOS-IV* models.

AOS model	*Property*	*Equation*	λ = 350 nm	λ = 450 nm	λ = 550 nm	λ = 650 nm
I, II, III, IV	ω_{mol} (λ)	*(15)*	1	1	1	1
I, III, IV	τ_{mol} (λ)	*(15)*	0.63031	0.22111	0.097069	0.049188
II			0	0	0	0

The TOA and SRF results in this study are for a detector located above below the atmosphere (see also **Fig. 1**).

Table 5b. Same as **Table 5a** except for *AOS-I** model.

AOS model	*Property*	*Equation*	λ ≈ 370 nm
*I**	ω_{mol} (λ)	(16)	1
	τ_{mol} (λ)	(17)	0.5

The TOA and SRF results in this study are for a detector located above below the atmosphere (see also **Fig. 1**).

Journal Pre-proof

Table 6. Summary of the RT code characteristics and options used to perform the RT computations.

	Topic	*Available option*	*eGAP*	*MarCh-AD*	*SOS-CAOS*	*SMART-G*	*Testbed Tables*
Computations	*RT method*	fixed (code-specific)	Adding-Doubling	Markov-Chain-Adding-Doubling	Successive Order of Scattering	Monte Carlo	Adding-Doubling
	AOS inhomogeneity	Vertical variations	yes	yes	yes	yes	Plane-parallel, horizontally homogeneous
		Horizontal variations	no	no	no	yes	
		Spherical shell	no	no	no	yes	
	Stokes vector	Scalar: *I* (ignore *Q*, *U*, *V*)	yes	yes	yes	no	Full Stokes vector
		3×3: *I*, *Q*, *U* (ignore *V*)	yes	yes	yes	no	
		Full: *I*, *Q*, *U*, *V*	yes	yes	yes	yes	
	AOS Reflection matrices	All scattering contributions	yes	yes	yes	yes	All scattering contributions
		Scattering decomposition[§]	yes	no	yes	no	
	Light propagation	Gaussian streams	yes	yes	yes	yes	Decoupled & non-Gaussian Streams
		Add non-Gaussian streams	yes	yes	yes	yes	
		Decouple sky-ocean streams	yes	no	yes	no	
	Accuracy	User-prescribed	yes	no [†]	no [†]	no [†]	10^{-5} - 10^{-6} [‡]
Atmosphere	*Molecular scattering and absorption*	Classic Rayleigh	yes	yes	yes	yes	Classic Rayleigh
		Depolarization	yes	yes	yes	yes	
		Inelastic	no	no	no	no	
	Aerosol scattering and absorption	Classic Mie	yes	yes	yes	yes	*none*
		Randomly oriented shapes	yes	yes	yes	yes	
		Oriented shapes	no	no	no	yes	
		Conservation of energy	yes	yes	yes	yes	
	Cloud scattering and absorption	Classic Mie	yes	yes	yes	yes	*none*
		Randomly oriented shapes	yes	yes	yes	yes	
		Oriented shapes	no	no	no	yes	
		Conservation of energy	yes	yes	yes	yes	
Oc	*Wave roughness*	Smooth (flat surface)	no	no	yes	yes	Isotropic

Journal Pre-proof

		Isotropic	yes	yes	yes	yes	
		Anisotropic	yes	yes	yes	no	
	Wave scattering	Geometrical optics approach	yes	yes	yes	yes	Geometrical optics approach
		BRDF surface approach	no	yes	yes	yes	
		Foam (Lambertian)	yes	yes	yes	yes	
		Wave shadowing	yes	yes	yes	fixed/yes □	
		Energy conservation	yes	yes	yes	fixed/yes □	
Ocean body	*Molecular scattering and absorption*	Classic Rayleigh	yes	yes	yes	yes	Classic Rayleigh
		Depolarization	yes	yes	yes	yes	
		Inelastic	no	no	yes	no	
	Hydrosol scattering and absorption	Classic Mie	yes	yes	yes	yes	Classic Mie & energy conservation
		Randomly oriented shapes	yes	yes	yes	yes	
		Oriented shapes	no	no	no	yes	
		Energy conservation	yes	yes	yes	yes	
	Bottom	Surface (Lambertian)	yes	yes	yes	yes	*none*

§ Scattering contribution from *(i)* atmosphere, *(ii)* sun-glint, *(iii)* atmosphere + surface, *(iv)* water-leaving radiance, *(v)* residual

† User can control (but not prescribe) accuracy by specifying stream number, Fourier terms, and sublayer optical thickness (*MarCh-AD*, *SOS-COART*), or the number of photons (*SMART-G*)

‡ For each AOS model, based on comparison of corresponding RT code results for all altitudes, wavelengths, and scattering geometry

□ Fixed (included) when using geometric optics to model ocean surface, optional when using BRDF to model ocean surface reflection

Journal Pre-proof

Declaration of interests

☒ The authors declare that they have no known competing financial interests or personal relationships that could have appeared to influence the work reported in this paper.

☐The authors declare the following financial interests/personal relationships which may be considered as potential competing interests:

Journal Pre-proof